JGR Solid Earth

RESEARCH ARTICLE
10.1029/2025JB031503

Seismic Source Spectral Properties of Dynamic Rupture With a Self-Similar, Self-Healing Slip Pulse: Origins of Double-Corner Displacement Spectra and Implications for Small Earthquake Rupture Modes

Yuto Kano[1], Yoshihiro Kaneko[1], and Peter M. Shearer[2]

[1]Graduate School of Science, Kyoto University, Kyoto, Japan, [2]University of California – San Diego, San Diego, CA, USA

Key Points:

- We develop fundamental rupture models characterized by self-similar, self-healing slip pulses and analyze their spectral characteristics
- Double-corner spectra arise from slip-pulse width, rupture directivity, gradual rupture arrest, slip heterogeneity, or Mach waves
- Our results indicate small- to moderate-size earthquakes may exhibit pulse-like rupture behavior

Supporting Information:

Supporting Information may be found in the online version of this article.

Correspondence to:

Y. Kaneko,
kaneko.yoshihiro.4e@kyoto-u.ac.jp

Citation:

Kano, Y., Kaneko, Y., & Shearer, P. M. (2025). Seismic source spectral properties of dynamic rupture with a self-similar, self-healing slip pulse: Origins of double-corner displacement spectra and implications for small earthquake rupture modes. *Journal of Geophysical Research: Solid Earth*, *130*, e2025JB031503. https://doi.org/10.1029/2025JB031503

Received 5 MAR 2025
Accepted 21 NOV 2025

Author Contributions:

Conceptualization: Yuto Kano, Yoshihiro Kaneko, Peter M. Shearer
Data curation: Yuto Kano, Yoshihiro Kaneko
Formal analysis: Yuto Kano, Yoshihiro Kaneko, Peter M. Shearer
Funding acquisition: Yoshihiro Kaneko
Investigation: Yuto Kano, Yoshihiro Kaneko, Peter M. Shearer
Methodology: Yuto Kano, Yoshihiro Kaneko, Peter M. Shearer
Project administration: Yoshihiro Kaneko
Resources: Yoshihiro Kaneko
Software: Yuto Kano, Yoshihiro Kaneko, Peter M. Shearer

Abstract We investigate the spectral characteristics and source properties of earthquake rupture models with self-similar, self-healing slip pulses. We compare pulse-like and crack-like rupture models across various idealized and heterogeneous source scenarios to identify conditions under which far-field displacement spectra characterized by two corner frequencies (double-corner frequency spectra) emerge. Five primary mechanisms are identified as causes of second high-frequency corners: (a) slip-pulse width, (b) rupture directivity, (c) gradual rupture arrest, (d) characteristic length of slip heterogeneity, and (e) Mach waves from supershear rupture. Spectra associated with slip-pulse width are most evident at small take-off angles from the fault normal, while those linked to rupture directivity and characteristic slip heterogeneity appear at large take-off angles. Estimated stress drops depend strongly on rupture mode and speed. Pulse-like models exhibit greater variability in estimated stress drops due to unknown rupture speeds than crack models, with pulse-like ruptures systematically underestimating moment-based stress drops by up to 40%. Comparisons to a recent study of Mw 3.0 to 5.5 earthquakes in Japan indicate a relationship between normalized corner frequency and scaled energy that fits better with pulse-like rupture models than with crack models, indicating small- to moderate-size earthquakes predominantly exhibit pulse-like rupture behavior. The gradual rupture arrest mechanism can produce double-corner spectra; however, it is unlikely to represent realistic earthquake sources due to its ω^{-3} spectral decay. Our results highlight the importance of incorporating pulse-like rupture dynamics into source models and point out challenges in interpreting source spectra and stress drop estimates when rupture characteristics are uncertain.

Plain Language Summary Earthquakes release seismic waves through ruptures along faults, and understanding the details of these ruptures helps us better interpret seismic data. This study examines two types of earthquake rupture behaviors: "pulse-like," where the fault slip stops quickly, and "crack-like," where it continues until the rupture reaches the fault's edge. By simulating various scenarios, we identify conditions that produce unique "double-corner" frequency patterns in seismic waveforms. These patterns can result from factors such as slip-pulse width, rupture speed, fault slip heterogeneity, or the effects of supershear rupture. Our findings show that pulse-like ruptures better match observed seismic energy patterns than crack-like ruptures, indicating that small- to moderate-size earthquakes often exhibit pulse-like behavior. However, estimating earthquake stress drops is challenging, as pulse-like ruptures introduce more variability than crack-like models. These results highlight the importance of considering pulse-like dynamics when modeling earthquakes and interpreting seismic data.

1. Introduction

Earthquakes may exhibit two primary rupture modes: a crack-like mode, where the local slip duration on the fault is comparable to the overall rupture duration, and a pulse-like mode, where the local slip duration is much shorter than the rupture duration (Heaton, 1990; Nielsen & Madariaga, 2003). While large earthquakes typically exhibit pulse-like rupture behavior (Kearse & Kaneko, 2025; Melgar & Hayes, 2017), it is not yet clear whether small earthquakes predominantly follow crack- or pulse-like rupture modes due to limited resolution within the rupture zones. Furthermore, the physical mechanisms responsible for arresting local slip and generating pulse-like ruptures are still not fully understood. Proposed explanations include self-healing slip governed by velocity-dependent friction (Heaton, 1990), stopping phases generated at fault strength barriers (Day, 1982), and processes occurring within the fault damage zone (Huang & Ampuero, 2011).

Supervision: Yoshihiro Kaneko
Validation: Yuto Kano, Yoshihiro Kaneko, Peter M. Shearer
Visualization: Yuto Kano, Yoshihiro Kaneko
Writing – original draft: Yuto Kano, Yoshihiro Kaneko
Writing – review & editing: Yuto Kano, Yoshihiro Kaneko, Peter M. Shearer

Assuming self-similarity of earthquakes, where stress drop and scaled energy are independent of earthquake size, small earthquakes would exhibit rupture characteristics similar to those of larger events. Consequently, most small earthquakes may follow a pulse-like rupture mode, analogous to their larger counterparts.

Nevertheless, theoretical models based on crack-like rupture behavior are widely used to infer the source properties of small earthquakes. For an elliptical crack in a homogeneous elastic medium, stress drop $\Delta\sigma$ of an earthquake can be expressed as

$$\Delta\sigma = C(a,b,\nu)\frac{M_0}{bS}, \tag{1}$$

where $C(a,b,\nu)$ represents a geometrical parameter determined by the major and minor axes (a and b) of the ellipse, ν is Poisson's ratio, M_0 is the seismic moment, and S denotes the source area (Eshelby, 1957; Madariaga, 1977). In the case of a circular source of a radius a within a Poissonian solid (i.e., $\nu = 0.25$), Equation 1 simplifies to

$$\Delta\sigma = \frac{7}{16}\frac{M_0}{a^3}. \tag{2}$$

Since direct measurement of source dimensions is typically infeasible, $\Delta\sigma$ is estimated from far-field body wave spectra by measuring the corner frequency f_c and employing a theoretical model of circular rupture. Assuming a theoretical rupture model, the source radius a can be linked to the spherical average of corner frequencies $\overline{f_c}$ in body wave seismic spectra using the relationship

$$\overline{f_c} = k\frac{\beta}{a}, \tag{3}$$

where β is the S-wave speed and k is a constant that depends on the wave type (P or S waves) and the specific theoretical circular rupture model, including rupture speed and source complexity (e.g., Brune, 1970; Kaneko & Shearer, 2014; Madariaga, 1976; Sato & Hirasawa, 1973). Combining Equations 2 and 3, the stress drop can be estimated via

$$\Delta\sigma = \frac{7}{16}\left(\frac{\overline{f_c}}{k\beta}\right)^3 M_0. \tag{4}$$

Numerous observational studies have estimated stress drops for small to moderate earthquakes using Equation 4 (e.g., Abercrombie, 1995; Abercrombie, 2014, 2015; Abercrombie, 2021; Allmann & Shearer, 2009; Calderoni & Abercrombie, 2023; Huang et al., 2017; Lin & Lapusta, 2018; McGuire & Kaneko, 2018; Shearer et al., 2022). Shearer et al. (2022) used a P-wave spectral decomposition approach to measure $\overline{f_c}$ and M_0, assumed k derived from Kaneko and Shearer (2014), and estimated stress drops for $M1.5$–$M4$ earthquakes in southern California from 1996 to 2019. They observed significant spatial variability in median stress drops and deviations from a self-similar model for $M > 3$ events. This deviation was attributed to trade-offs between the assumed high-frequency falloff rate and corner frequency fitting. Abercrombie (2021) compiled source parameter measurements from various studies, showing that within-study variations are comparable to those observed across different studies. This variability likely stems from differences in spectral fitting methods, actual stress variations, and assumptions inherent in source models (e.g., Baltay et al., 2025; Neely et al., 2025). Understanding the factors contributing to this variability remains an unresolved challenge.

Dynamic source models that quantify the value of k in Equation 3 are largely based on crack models (e.g., Brune, 1970; Kaneko & Shearer, 2014; Madariaga, 1976; Sato & Hirasawa, 1973). For instance, Brune (1970) proposed a simplified kinematic model for a circular fault, resulting in $k = 0.37$ for S waves. Sato and Hirasawa (1973) applied Eshelby's static solution (Eshelby, 1957), assuming radially propagating rupture that halts abruptly at the source radius, resulting in $k^P = 0.44$ and $k^S = 0.32$ for rupture speed $V_r = 0.9\beta$. However, this model assumes instantaneous cessation of slip across the entire fault plane, which is unphysical. Madariaga (1976) simulated a dynamic singular crack model with spontaneous healing of slip and found $k^P = 0.32$ and

Table 1
Comparison of k^P and k^S Values From This Study With Those From Previous Studies

	Crack model							Pulse model			
V_r/β	k^S_{Brune}	$k^P_{S\&H}$	$k^S_{S\&H}$	k^P_{Mada}	k^S_{Mada}	$k^P_{K\&S}$	$k^S_{K\&S}$	$k^P_{W\&D}$	$k^S_{W\&D}$	k^P	k^S
Infinite	0.37										
0.9		0.44	0.32	0.32	0.21	0.38	0.26			0.50	0.39
0.83								0.40	0.36		
0.8		0.41	0.30			0.35	0.26			0.45	0.42
0.7		0.39	0.29			0.32	0.26			0.39	0.38
0.6		0.34	0.27			0.30	0.25			0.34	0.33

Note. Subscripts Brune, S&H, Mada, K&S, and W&D correspond to the models of Brune (1970), Sato and Hirasawa (1973), Madariaga (1976), Kaneko and Shearer (2014), and Wang and Day (2017), respectively.

$k^S = 0.21$ for $V_r = 0.9\beta$. Kaneko and Shearer (2014) investigated cohesive-zone models of a circular fault in the small-scale yielding limit and numerically determined that the values of $k^P = 0.38$ and $k^S = 0.26$ for the singular crack model with spontaneous slip healing and $V_r = 0.9\beta$ are greater than those estimated by Madariaga (1976). Different k values reported in previous studies are summarized in Table 1. Clearly, any uncertainty in k in Equation 4 is magnified by being cubed when computing the stress drop. Furthermore, the inference of the underlying source process using Equation 4 is inherently tied to the assumed crack-like model through the specific choice of k.

More recently, Wang and Day (2017) simulated pulse-like ruptures on a fault governed by rate and state dependent friction laws with enhanced weakening and derived $k^P = 0.40$ and $k^S = 0.36$ for the growing pulse scenario, where the peak of the local slip rate increases with distance from the center of the fault. Assuming the values of k^S in Wang and Day (2017), the estimated stress drop via Equation 4 yields a stress drop 5.0 times smaller than that based on the crack model of Madariaga (1976). The pulse-like rupture models of Wang and Day (2017) also showed the appearance of a second, high-frequency corner in the stacked displacement spectra, which could be interpreted as indicative of pulse width. However, due to the artificial nucleation patch and the non-self-similar nature of their source models, generalization and applications to earthquakes of varying sizes remain uncertain. For example, the assumption of quasi-constant pulse widths cannot be applied to model earthquakes of different magnitudes (e.g., M2 vs. M5). One way to address this limitation is to consider a self-similar, self-healing slip pulse model developed by Nielsen and Madariaga (2003). However, due to its two-dimensional nature, this model is not well suited for analyzing or comparing the resulting spectral characteristics of waveforms with observations.

Many observational studies have noted discrepancies between observed earthquake spectra and the Brune model, which is characterized by a smooth spectrum with a single corner frequency and f^{-2} falloff in displacement at high frequencies. Deviations for individual earthquakes are often attributed to source complexity (e.g., Abercrombie, 2021; Neely et al., 2025), but a growing number of studies have found evidence for double-corner frequency models with an intermediate falloff rate considerably less than f^{-2} between the lower and upper corner frequencies (e.g., Archuleta & Ji, 2016; Atkinson, 1993; Atkinson & Silva, 1997, 2000; Boatwright & Choy, 1992; Boore et al., 2014; Denolle & Shearer, 2016; García et al., 2004; Izutani, 1984; Ji & Archuleta, 2020; Luco, 1985; Shimmoto & Miyake, 2025). Further support for an intermediate falloff rate above a lower corner frequency has come from the global earthquake analyses of Allmann and Shearer (2009) and Ye et al. (2016), who found high-frequency falloffs averaging $f^{-1.6}$ in teleseismic data, but did not have the bandwidth to resolve a possible second corner frequency.

Observations of spectra with double corner frequencies are often interpreted using Haskell's kinematic model (Haskell, 1964), which attributes the two corners to distinct time scales associated with the local rise time and the total rupture duration. However, the Haskell model assumes a line source that initiates abruptly and does not account for the effects of stopping phases from the top and bottom edges of the fault on slip arrest, making it somewhat unphysical. Many possible explanations have been proposed for the existence of a second, higher

corner frequency, including fault width (e.g., Savage, 1972), models involving asperities or multiple subevents (e.g., Atkinson & Silva, 2000; Boatwright, 1988; Boatwright & Choy, 1992; Luco, 1985), and models of a propagating slip pulse of limited duration (e.g., Bernard et al., 1996; Denolle & Shearer, 2016; Gusev, 2013; Ji & Archuleta, 2020; Wang & Day, 2017). Consequently, the origin and occurrence rate of the second high-frequency corner remain unclear.

To address these issues, we develop idealized, three-dimensional source models of earthquake rupture featuring a self-similar, self-healing slip pulse and analyze the resulting far-field displacements and spectra. Motivated by observational studies reporting invariant stress drops and scaled energy over a wide range of earthquake magnitudes, we adopt self-similar slip-pulse models as the logical basis of our analysis. The setup of the source models is detailed in Section 2. Section 3 compares the spectral characteristics and estimated stress drops of representative pulse models with those of the crack models. In Section 4, we explore the occurrence of double-corner frequency spectra across various rupture modes, geometries, and rupture velocities. Additionally, we examine more complex source scenarios, such as spontaneous rupture arrest and heterogeneous fault conditions, in Sections 5 and 6. Finally, in Section 7, we discuss the implications of our findings for interpreting small to moderate earthquakes.

2. Model Setting

We consider circular and elliptical faults embedded in an infinite, homogeneous, isotropic elastic medium (Figures 1a, 1c, and 1d). To create a source model of expanding rupture with a self-healing slip pulse, we extend the formulation of Kaneko and Shearer (2014); Kaneko and Shearer (2015), in which the shear strength τ_{st} of the fault weakens at a rate A_w within the cohesive zone and τ_{st} increases at a rate A_h with distance behind the healing front:

$$\tau_{st} = \max\{\tau_d - A_h(|r| - V_h t), \tau_d, \tau_d + A_w(|r| - V_r t)\}, \quad (5)$$

where τ_d is the dynamic shear strength, V_r is the rupture speed, V_h is the healing front speed, (Figure 1b). This parametrization leads to pulse-like rupture with a self-similar, self-healing slip pulse. Initially, the fault is subjected to a shear stress τ_0 and remains stationary until the shear stress reaches the fault strength τ_p. The value of τ_p is not predetermined but is influenced by the dynamic strength τ_d and the weakening rate A_w (Figure 1b). During slip, shear stress equals shear strength and increases after the healing front passes, arresting slip behind the rupture. Unlike crack models that lead to stress overshoot (Kaneko & Shearer, 2014), the pulse model results in stress undershooting that occurs behind the healing front (Figure S1 in Supporting Information S1).

We first focus on a circular symmetrical model (Figure 1a), where the rupture nucleates at the center of the fault and expands at a constant speed V_r. Rupture growth stops instantaneously when it reaches the zone of zero shear stress beyond the source radius a (Figure 1a). The level of shear stress beyond the circular source is set much lower than the dynamic strength τ_d. For simplicity, V_r is fixed, but the model remains dynamic as fault motion is calculated based on the assumed V_r and prescribed dynamic stress drop $\Delta\sigma_d$ (sometimes called effective stress). If the weakening rate A_h is too small, rupture will not stop behind the healing front, preventing the generation of a pulse-like rupture. The final stress increases slightly at the fault center due to the increase in shear strength (Figure 2h). We adjust A_h to minimize this stress increase at the center of the circular fault.

We also consider an asymmetrical model (Figure 1c), where rupture initiates at the edge of the circular fault, as well as a symmetrical elliptical model (Figure 1d) to account for supershear rupture. In the elliptical model, rupture propagates at varying speeds in different directions.

The elastodynamic equation, combined with the frictional weakening criterion (Equation 5), is solved using the spectral element method (Kaneko et al., 2008, 2011; Komatitsch & Vilotte, 1998). The computational domain is sufficiently large to prevent interference from waves reflected at the boundaries. For simplicity, we numerically solve for the x-component of slip and shear traction without rake rotation, even as the elliptical rupture front propagates. To achieve well-resolved numerical results, a minimum of 7–10 computational node points are allocated within the cohesive zone. The spectral element model includes artificial viscosity in the Kelvin-Voigt form to mitigate spurious oscillations generated by fault slip at frequencies beyond the resolution capability of the

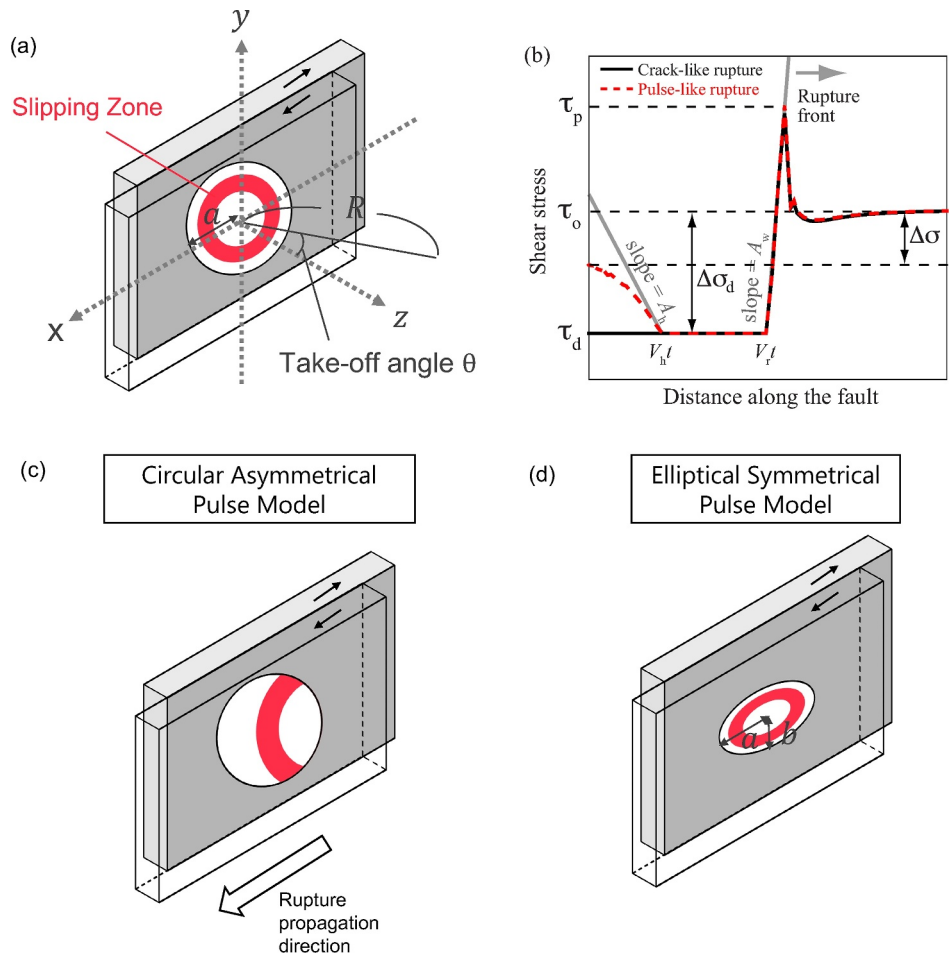

Figure 1. Model geometry and fault constitutive response. (a) A circular fault with a radius a embedded in an infinite medium. Uniform prestress τ_0 is imposed within a circular fault patch, with zero prestress outside the patch. (b) Fracture criterion in this study (red dashed line) and crack model assumed in Kaneko and Shearer (2014) (black line). Shear strength increases linearly from position $V_r t$ (as shown by a gray line) within the cohesive zone. Slip begins when the shear stress τ on the fault reaches the shear strength τ_p and stops behind the healing front, where the distance from the center of the fault exceeds $V_h t$. (c) Schematic diagram of the circular asymmetrical model. (d) Schematic diagram of the elliptical symmetrical model.

mesh. The dynamic rupture code has been verified through a series of verification exercises (Harris et al., 2009, 2011).

Dimensional analysis enables representation of solutions in terms of nondimensional variables. We adopt the following nondimensionalizations, similar to Kaneko and Shearer (2014); Kaneko and Shearer (2015), for the circular model:

$$\text{Length } r' = r/a \tag{6}$$

$$\text{Time } t' = t/a \tag{7}$$

$$\text{Stress } \sigma'_{ij} = \sigma_{ij}/\Delta\sigma_d \tag{8}$$

$$\text{Displacement } u'_i = u_i\mu/(\Delta\sigma_d a) \tag{9}$$

$$\text{Weakening Rate } A'_w = A_w a/\Delta\sigma_d \tag{10}$$

$$\text{Healing Rate } A'_h = A_h a/\Delta\sigma_d \tag{11}$$

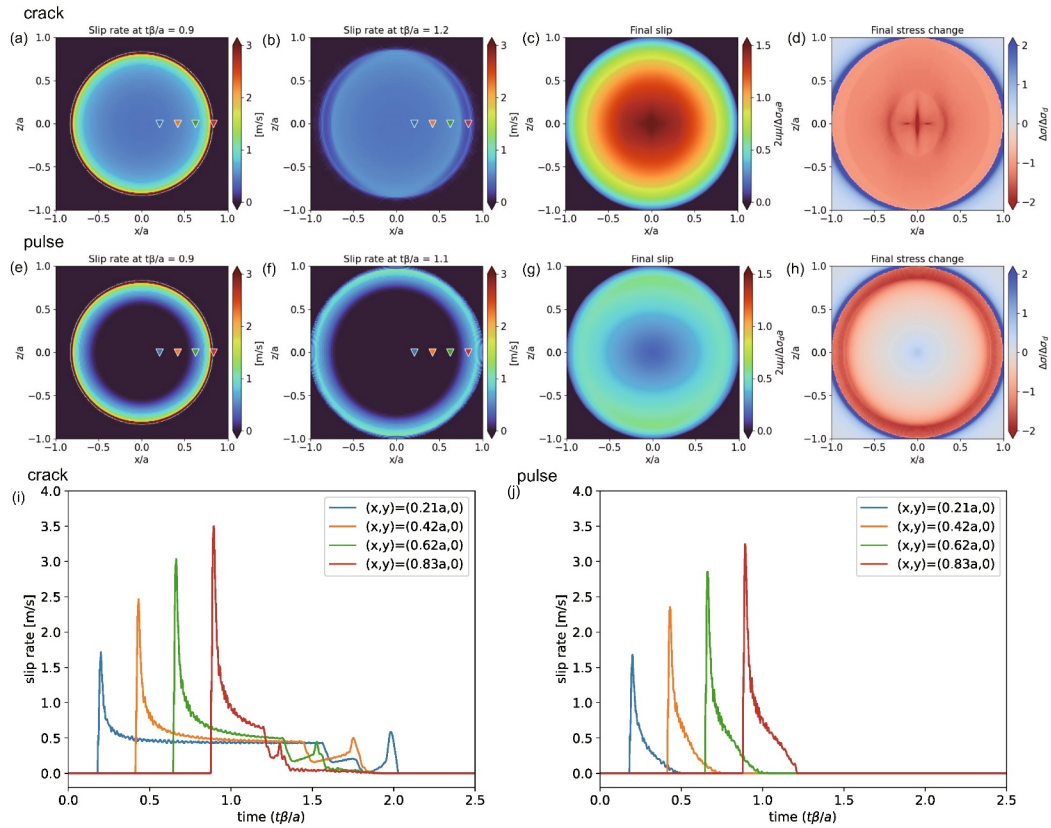

Figure 2. Comparison of source characteristics between the crack model with $V_r = 0.9\beta$ and the pulse model with $V_r = 0.9\beta$ and $V_h = 0.7\beta$. (a, b, e, f) Snapshots of slip-rate distribution. Triangles represent the stations used to record the slip rate functions in panels (i and j). (c, g) Final slip distribution. (d, h) Final stress change distribution on the fault. (i, j) Slip rate as a function of time at several points on the fault.

$$\text{Seismic Moment } M_0' = M_0/\left(\Delta\sigma_d(a)^3\right) \tag{12}$$

$$\text{Radiated Energy } E_r' = E\mu/\left(\Delta\sigma_d^2(a)^3\right), \tag{13}$$

where nondimensional variables are denoted by a prime. The physical variables considered are the source radius a, the dynamic stress drop $\Delta\sigma_d$, the S wave speed β, and the shear modulus μ. Poisson's ratio is assumed to be 0.25, such that $\alpha = \sqrt{3}\beta$.

3. Comparison Between Crack Versus Pulse Models: A Circular Fault

In this section, we compare the characteristics of the circular pulse models with those of circular crack models, as described by Kaneko and Shearer (2014, 2015). Unless otherwise specified, we set $A_w' = 84$ and $A_h' = 4.2$.

3.1. Source Characteristics

Figure 2 compares representative crack and pulse models in terms of slip rate, final slip, and final stress change. In the crack model, the fault continues to slip until the arrival of stopping phases due to the sudden rupture arrest at the fault edge. In the pulse model, slip stops spontaneously, driven primarily by the tail of the self-healing slip pulse, but the fault also experiences stopping phases produced at its edge (Figure 2). The peak slip rate in the pulse model increases from the center to the edge, a feature consistent with the growing pulse model described by Wang and Day (2017) (Figure 2f). The slip rate amplitude scales approximately with the square root of distance (Figure 2j), consistent with a self-similar, expanding circular shear crack (Kostrov, 1964). The local slip duration is shorter in the pulse model compared to the crack model. On average, slip in the pulse model is smaller than that

in the crack model (Figures 2c and 2g), as the slip duration is shorter in the pulse model than in the crack model. In the pulse model, the shear stress at the center of the fault slightly increases due to its self-healing nature (Figure 2h). Note that differences in source behavior along the Mode II and Mode III directions lead to slight asymmetries in the results. Compared to the crack model, the moment-rate function in the pulse model decays more rapidly from its peak due to a more abrupt slip arrest (Figures S2a and S2b in Supporting Information S1). Overall, these source characteristics of the pulse model are similar to those in the growing pulse model of Wang and Day (2017).

3.2. Spectral Properties

Far-field body wave displacement across the focal sphere in a homogeneous elastic whole space is computed from fault source-time histories derived from the rupture model. The far-field body-wave displacement by a shear dislocation at an individual fault patch is expressed as

$$\boldsymbol{u}(\boldsymbol{x},t) = \frac{1}{4\pi\rho\alpha^3}\boldsymbol{A}^P\frac{1}{R}\dot{M}_0\left(t-\frac{R}{\alpha}\right) + \frac{1}{4\pi\rho\beta^3}\boldsymbol{A}^S\frac{1}{R}\dot{M}_0\left(t-\frac{R}{\beta}\right), \tag{14}$$

where ρ is the density, $\dot{M}_0$ is the moment rate, R is the distance from the source to the receiver, and $\boldsymbol{A}^{\mathrm{P}}$ and $\boldsymbol{A}^{\mathrm{S}}$ account for the radiation patterns for far-field P and S waves, respectively (Aki & Richards, 2002). We set $R = 166a \gg a$, to satisfy the far-field assumption. Finite-source effects are included by summing $\boldsymbol{u}(\boldsymbol{x},t)$ over all grid points. Attenuation and scattering are neglected to isolate source effects.

The corresponding spectrum is derived by applying the Fourier transform to the magnitude of the far-field displacement, $|\boldsymbol{u}(\boldsymbol{x},t)|$, at each receiver. For S waves, the far-field displacements and spectra are calculated for the norm of the SH and SV waves. The corner frequency and spectral fall-off rate are estimated by fitting a Brune-type spectral function (Brune, 1970) to an individual spectrum:

$$U(f) = \frac{\Omega_0}{1+\left(f/f_c\right)^n}, \tag{15}$$

where Ω_0 represents the long-period spectral level proportional to the seismic moment M_0, f_c denotes the corner frequency, and n specifies the spectral fall-off rate. The parameters f_c and n are determined by performing a least-squares fit on the logarithmic spectrum over the frequency range, $0.05f_c \lesssim f \lesssim 20f_c$ using a grid-search method. This range differs slightly from Kaneko and Shearer (2014, 2015) to emphasize higher frequencies. We weight the fit inversely by frequency, ensuring equal contribution across the spectrum in a log-log plot. This enhances the fit for the low-frequency portion of the spectrum, which typically has fewer data points. Spectra and f_c are computed at 5° intervals across the focal sphere. The take-off angle θ is measured from the fault normal direction (Figure 1a). The normalized corner frequency f_c' is expressed as

$$f_c' = f_c\frac{a}{\beta}. \tag{16}$$

We compare and identify the characteristics of far-field S-wave displacement spectra between the crack and pulse models. Figure 3 illustrates far-field S-wave displacements and spectra at receivers with different take-off angles. In the crack model, the spectra are predominantly well-represented by a Brune-type spectral function (Figure 3a). In contrast, spectra in the pulse model exhibit the emergence of a second corner frequency at higher frequencies at several receivers, marked by deviations from single-corner spectral fitting (Figure 3b).

Two mechanisms explain the second corner in pulse-model spectra. At small take-off angles (normal to the fault plane), it reflects the slip-pulse width of the propagating rupture (e.g., 0.5° in Figure 3b), corresponding to the duration of the slip pulse before reaching the fault edge. At large take-off angles (e.g., 60°, 89.5°), the second corner arises from rupture directivity effects (Figure 4). The rising part of the displacement corresponds to the rupture's arrival at the nearest edge of the fault, while the return to zero marks the arrival of the S wave from the farthest edge (Figures 3b and 4). As discussed in detail later, the second corner frequency in the spectra reflects the rising portion of the far-field displacement caused by rupture directivity effects, which enhance the intermediate frequency range and produce the second corner (Figure 4). Notably, a second corner also appears at large take-off

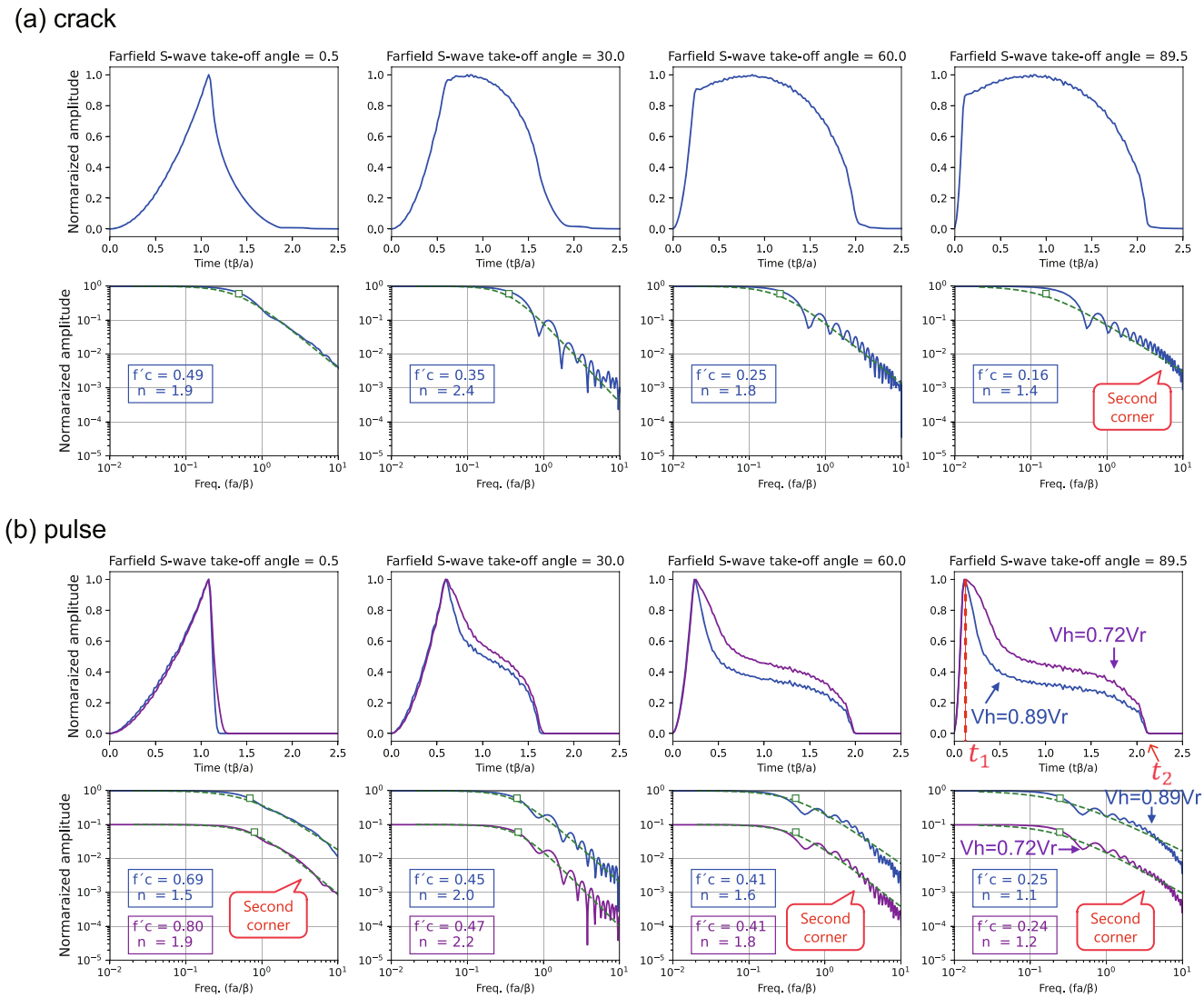

Figure 3. Far-field S-wave displacements (upper) and corresponding spectra (lower) at four take-off angles for (a) the crack model with $V_r = 0.9\beta$ and (b) pulse models with $V_r = 0.9\beta$ and $V_h = 0.89V_r$ (blue lines) or $V_h = 0.72V_r$ (purple lines). Spectra for the $V_h = 0.72V_r$ case are uniformly shifted vertically on the logarithmic axis for comparison. Corner frequencies are indicated by open squares. Green dashed lines show the best-fitting model of the Brune-type spectral function (Equation 15). Normalized corner frequencies f_c' and fall-off rates n are indicated in the boxes. The pulse models at small take-off angles from the fault normal (0.5°) and large take-off angle (60°, 89.5°) exhibit the double-corner frequency spectra.

angles in the crack model (Figure 3a), indicating that this feature is unrelated to slip pulse width. However, the effect is less pronounced compared to the pulse model.

To examine pulse width effects, we compare pulse models with different V_h (Figure 3b). Compared to the model with $V_h = 0.89V_r$ (blue line in Figure 3b), the model with $V_h = 0.72V_r$ (purple line in Figure 3b), which has a larger pulse width, exhibits a longer slip duration and, consequently, a larger displacement amplitude. At receivers with small take-off angles, waves from the edges of the circular fault arrive almost simultaneously, resulting in a simple waveform. The portion of the displacement that drops from the peak to zero corresponds to the duration of slip arrest after the rupture front reaches the edge of the fault. This duration is longer and the resulting second corner frequency is smaller for the model with $V_h = 0.72V_r$ (model with larger pulse width) (Figure 3b). At large take-off angles, the second corner frequencies are nearly identical across models with different pulse widths, indicating that this second corner frequency is unrelated to the pulse width. The emergence of second corners is discussed in greater detail in Section 4.1.

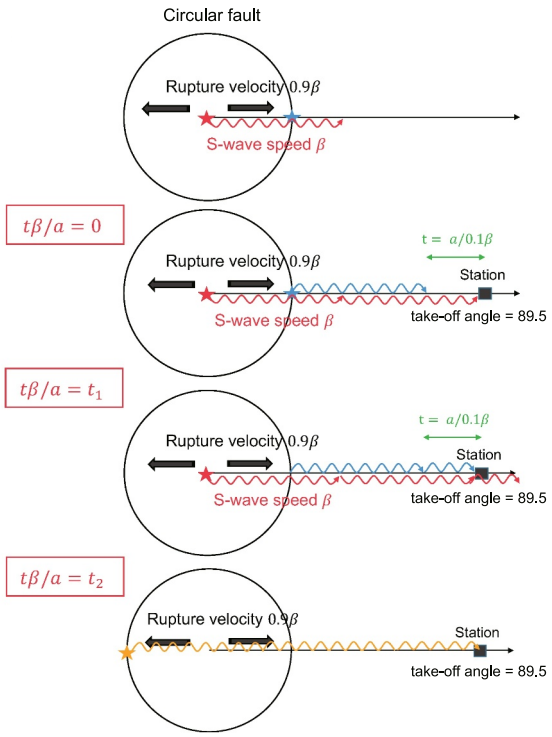

Figure 4. Schematic illustration of the directivity effect discussed in the main text. At $t\beta/a = 0$, the S-wave first arrives at a station located in the direction of rupture propagation ($\theta \approx 90°$). At $t\beta/a = t_1$, the stopping phase from the nearest edge of the fault arrives, initiating a decrease in displacement (as shown in Figure 3b). During the interval $t_1 < t < t_2$, stopping phases from the circular edge of the fault arrive successively, further reducing the displacement. At $t\beta/a = t_2$, the stopping phase from the farthest edge arrives, returning the displacement to zero (also indicated in Figure 3b). The rising part of the displacement during the interval $0 < t < t_1$ controls the spectral amplitude in the intermediate frequency band, characterized by an $\omega^{-1.5}$ decay.

Figure S3 in Supporting Information S1 illustrates the far-field P-wave displacements and spectra for both the circular symmetrical crack and pulse models. The key difference between P-wave and S-wave spectra lies in the influence of rupture directivity. Since P waves travel faster than S waves, the relative difference between the rupture speed and the P-wave speed is greater. As a result, the rising portion of the far-field waveform is more gradual, diminishing the effects of rupture directivity in the P-wave spectra. In both the crack model (Figure S3a in Supporting Information S1) and the pulse model (Figure S3b in Supporting Information S1), a double-corner frequency does not appear at high take-off angles (take-off angle = 60° or 89.5°) in the P-wave spectra. In contrast, for the pulse model, a second, high-frequency corner related to the pulse width is observed at lower take-off angles. These results suggest that double-corner frequency spectra attributed to the rupture directivity effects are exclusive to S-wave spectra, while double-corner frequencies resulting from the pulse width are present in both P- and S-wave spectra.

Figure 5 shows the spherical distributions of normalized corner frequency f_c' and fall-off rates. In the pulse model, f_c' values are larger at high latitudes and smaller at low latitudes, a pattern attributed to the rupture directivity effects. This characteristic is also observed in the crack model, though the rupture directivity effect is more pronounced in the pulse model. The spectral fall-off rate n is higher at higher latitudes, corresponding to the presence of double-corner frequency spectra. The relationships between the spherical averages of P- and S-wave corner frequencies and the source radius are shown as:

$$f_c^{\mathrm{P}} = k^{\mathrm{P}}\frac{\beta}{a}$$
$$f_c^{\mathrm{S}} = k^{\mathrm{S}}\frac{\beta}{a}, \tag{17}$$

where k denotes corner frequency normalized by β and a. We find that, for the pulse model, the spherical averages of the corner frequencies are $k^{\mathrm{P}} = 0.50$ and $k^{\mathrm{S}} = 0.39$, which are larger than $k^{\mathrm{P}} = 0.36$ and $k^{\mathrm{S}} = 0.26$ for the crack model (Figure 5). This reflects shorter slip duration in the pulse model. The

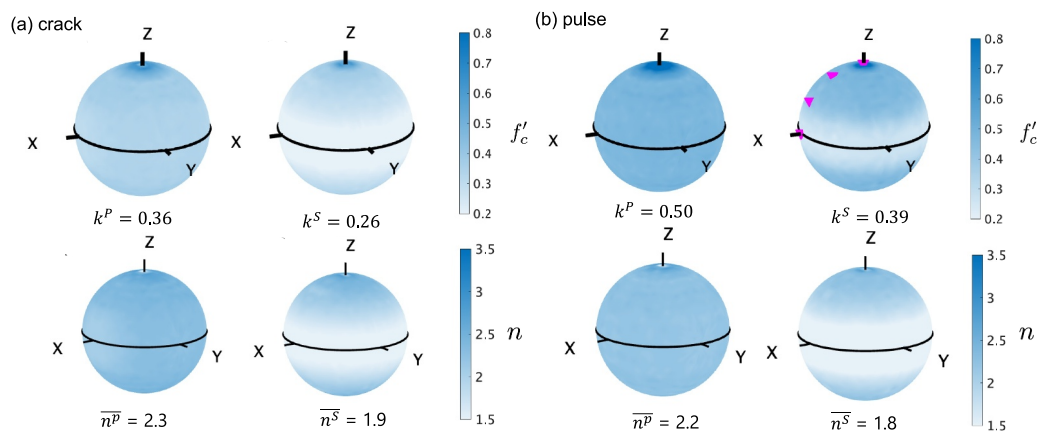

Figure 5. Spatial variations of normalized P- and S-wave corner frequencies f_c' and fall-off rates n over the focal sphere for (a) the circular crack model with $V_r = 0.9\beta$ and (b) the circular pulse model with rupture speed $V_r = 0.9\beta$ and $V_h = 0.7\beta$. The fault is along the X-Y plane. Magenta triangles indicate receiver locations where displacements and spectra are shown in Figure 3. The values of spherically averaged normalized corner frequency k^{P} and k^{S}, as well as fall-off rates n^{P} and n^{S} are indicated.

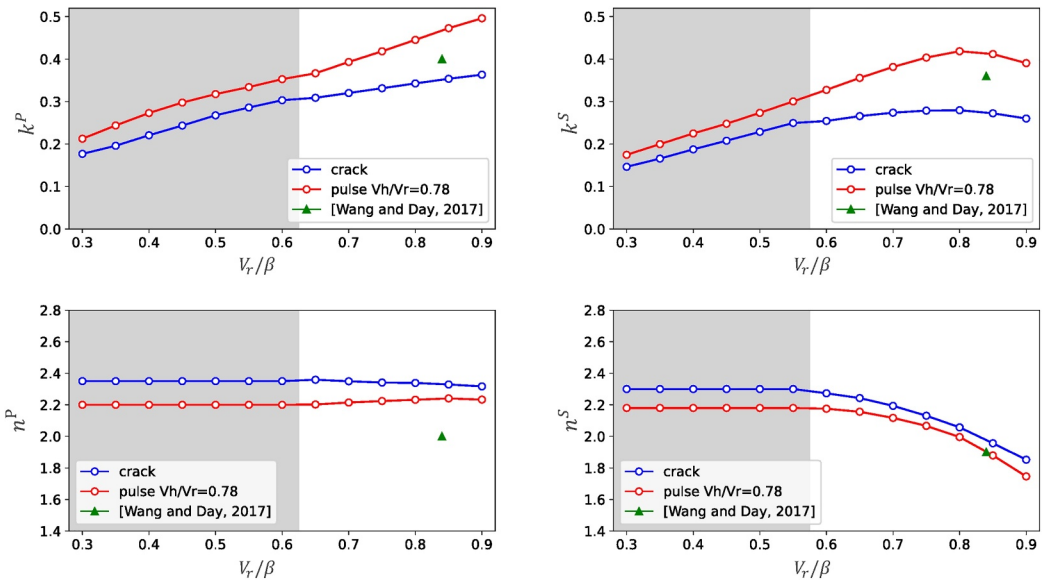

Figure 6. Rupture speed dependence of k^P, k^S, n^P, n^S. In the gray-shaded region, the fall-off rate is fixed to the average value from the case with variable fall-off rates to reduce the fitting bias effects. The value from the model of Wang and Day (2017), by averaging the rupture speeds along the in-plane (Mode II) and anti-plane (Mode III) directions, is shown as a green triangle. k^P and k^S generally increase with rupture speed.

mean fall-off rate $n \approx 2$ for both models agrees with Wang and Day (2017). The k^P and k^S values for the pulse model are larger than those in the growing pulse model of Wang and Day (2017) (Table 1). The larger k^P and k^S values for the pulse model may result from differences in rupture speed, nucleation procedures, or the non-self-similar nature of the source model assumed in Wang and Day (2017). Note that $k^P = 0.36$ and $k^S = 0.26$ for the crack model are slightly different from those reported in Kaneko and Shearer (2014) due to differences in the frequency range used for fitting.

3.3. Dependence of k_P and k_S on Rupture Velocity

Figure 6 illustrates the dependence of normalized corner frequencies (k^P, k^S) and fall-off rates (n^P, n^S) on rupture speeds. For cases with slow rupture speeds ($V_r \leq 0.6\beta$), the rupture stops more gradually at the fault's edge, leading to reduced dominance of high-frequency components in the spectra. Consequently, the fall-off rates increase and approach approximately 3. In such cases, fitting bias causes the corner frequencies to appear higher, necessitating the fixing of fall-off rates. Thus, in cases with slow rupture speeds (indicated by the gray area in Figure 6), the fall-off rates are fixed at $n^P = 2.35$ and $n^S = 2.30$ in the crack models, and $n^P = 2.20$ and $n^S = 2.18$ in the pulse models, respectively, during the corner frequency estimation.

The corner frequency generally increases with rupture speed, as expected (Figure 6), because fast rupture speeds result in shorter durations of far-field displacement. The variation in k values across different rupture speeds is approximately twice as large for the pulse models compared to the crack models. The k values obtained in this study are slightly larger than those reported by Wang and Day (2017) (Figure 6). For the S waves at fast rupture speeds, k^S decreases as rupture speed increases ($V_r/\beta \geq 0.8$) (Figure 6). This behavior is attributed to fitting bias caused by rupture directivity effects, which reduce the fall-off rate n and consequently lower the corner frequency during the fitting process.

3.4. Scaled Energy and Radiation Efficiency

We compare the scaled energy of the crack and pulse models. We quantify estimated radiated energy by analyzing the computed far-field spectra for both the pulse and crack models. In a uniform whole space, the far-field radiated S-wave energy is given by

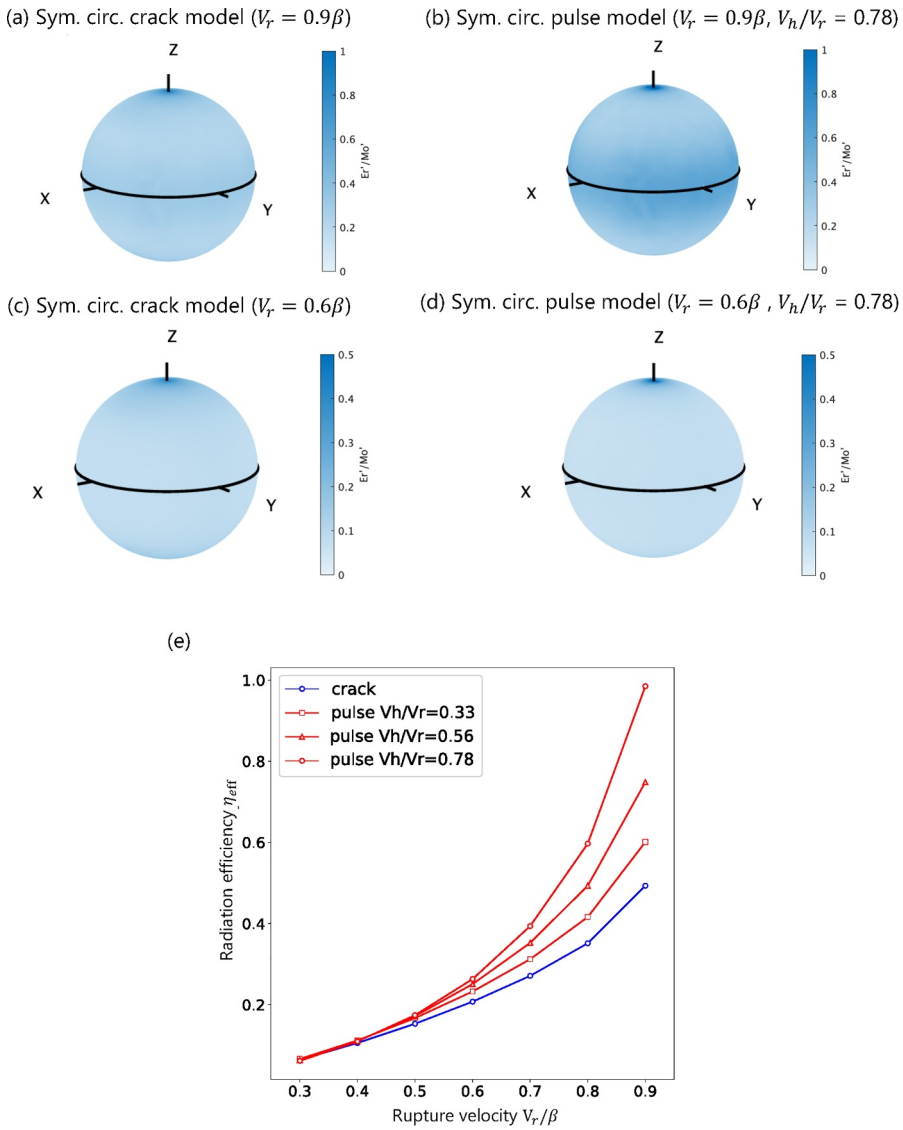

Figure 7. Comparison of scaled energy E_r'/M_0' across the focal sphere for (a) the circular crack model with $V_r = 0.9\beta$, (b) the circular pulse model with rupture speed $V_r = 0.9\beta$ and $V_h = 0.7\beta$, (c) the circular crack model with $V_r = 0.6\beta$, and (d) the circular pulse model with $V_r = 0.6\beta$. (e) Dependence of radiation efficiency on rupture speed for the crack model and pulse models with varying pulse widths. Radiation efficiency increases with rupture speed, with the pulse model exhibiting higher radiation efficiency than the crack model.

$$E_r^S = \frac{\langle \Psi_S^2 \rangle}{4\pi\rho\beta^5} M_0^2 \int_0^\infty |\omega A(\omega)|^2 d\omega, \tag{18}$$

where $\langle \Psi_S^2 \rangle$ represents the mean over the focal sphere of the radiation pattern Ψ_S (=2/5 for S waves), M_0 is the seismic moment, ω denotes the angular frequency, and $A(\omega)$ refers to the normalized displacement spectrum (Baltay et al., 2011; Mayeda & Walter, 1996). The non-dimensional scaled energy can be expressed as

$$\frac{E_r'^S}{M_0'} = \frac{E_r^S}{M_0} \frac{\mu}{\Delta\sigma_d} = \frac{\langle \Psi_S^2 \rangle}{4\pi\beta^3 \Delta\sigma_d} M_0 \int_0^\infty |\omega A(\omega)|^2 d\omega, \tag{19}$$

where μ is the shear modulus and $\Delta\sigma_d$ is the dynamic stress drop (Kaneko & Shearer, 2015).

Table 2
Source Parameters for the Rupture Models Considered in This Study

	V_r/β	k^P	k^S	k^P/k^S	$\Delta\sigma/\Delta\sigma_d$	E'_r/M'_0	η_{eff}
Sym.Circ.Pulse	0.6	0.34	0.33	1.0	0.75	0.10	0.26
	0.7	0.39	0.38	1.1	0.77	0.15	0.39
	0.8	0.45	0.42	1.1	0.80	0.24	0.60
	0.9	0.50	0.39	1.3	0.82	0.40	0.99
Asym.Circ.Pulse	0.6	0.23	0.21	1.1	0.74	0.06	0.16
	0.7	0.25	0.24	1.1	0.78	0.11	0.27
	0.8	0.29	0.28	1.0	0.82	0.20	0.48
	0.9	0.32	0.32	1.0	0.87	0.43	1.0
Sym.Ellip.Pulse	1.3	0.55	0.34	1.4	0.81	0.34	0.83
	1.6	0.59	0.40	1.5	0.81	0.45	1.1

Note. Results for the symmetrical circular pulse model (Sym.Circ.Pulse), asymmetrical circular pulse model (Asym.Circ.Pulse), symmetrical elliptical pulse model (Sym.Ellip.Pulse), are described in Sections 4.1–4.3, respectively. Spherical averages of P and S wave corner frequencies, k^P and k^S, stress drop $\Delta\sigma/\Delta\sigma_d$ (Equation 2), scaled energy E'_r/M'_0, and radiation efficiency η_{eff} are reported.

Figure 7a–7d show spherical plots of scaled energy E'_r/M'_0, with the corresponding values listed in Table 2. In the crack model with $V_r = 0.9\beta$ (Figure 7a), the estimated scaled energy exhibits little variation across the focal sphere, consistent with previous findings (Kaneko & Shearer, 2015). In contrast, the pulse model with $V_r = 0.9\beta$ (Figure 7b) shows moderate azimuthal variation, with larger scaled energy values near the equator. This difference arises because rupture directivity effects are more pronounced in the pulse model. However, for models with slower rupture speeds, the difference in scaled energy distribution between the crack and pulse models becomes negligible (Figures 7c and 7d).

Figure 7e illustrates radiation efficiency as a function of rupture speed. Radiation efficiency is defined as:

$$\eta_{eff} = \frac{2\mu E_r}{\Delta\sigma M_0}, \tag{20}$$

where is $\Delta\sigma$ is the static stress drop. To calculate radiation efficiency, we use the average static stress drop weighted by the final slip $\Delta\sigma_E$, as described by Noda et al. (2013):

$$\Delta\sigma_E = \frac{\int \Delta\sigma(x,y)D(x,y)dS}{\int D(x,y)dS}, \tag{21}$$

where $D(x,y)$ and $\Delta\sigma(x,y)$ are slip and stress change distributions over the fault area S.

Radiation efficiency increases with rupture speed in both models but more steeply for pulse ruptures. At high rupture speeds, the radiation efficiency of the pulse model exceeds that of the crack model, reaching ~1.0, whereas both models exhibit nearly identical values at slow rupture speeds (Figure 7e). The pulse model with a smaller pulse width achieves higher radiation efficiency due to more pronounced fault restrengthening (Figure 7e). In contrast, the crack model shows a nearly linear increase in radiation efficiency with rupture speed. The higher radiation efficiency observed in the pulse model at fast rupture speeds is attributed to prominent stress undershooting. These characteristics are compared with observations of small to moderate earthquakes in Section 7.

4. Double Corner Frequency Spectra in Crack and Pulse Models With Different Source Geometry and Rupture Velocity

To investigate the reasons behind the emergence of double-corner frequency spectra, we analyze the spectral properties of models with varying fault geometries and rupture propagation speeds. To quantify the appearance of the second corner frequency and its associated change in fall-off rates, we expand upon the method of Denolle and Shearer (2016) and introduce a double-corner frequency model for spectral fitting, as follows:

$$u(f) = \frac{\Omega_0}{\sqrt{1+(f/f_{c1})^n}\sqrt{1+(f/f_{c2})^n}}, \tag{22}$$

where f_{c1} and f_{c2} represent the first and second corner frequency, respectively. In the fitting model used by Denolle and Shearer (2016), n in Equation 22 is set to 2. However, in our approach, n is derived based on the Brune model spectrum (Equation 15) for sufficiently large f, where $f_{c1} \simeq f_{c2}$. Consequently, n represents the fall-off rate at high frequencies ($f \to \infty$) and is referred to as n_2. We then fit the spectra using a Brune-type spectral function via grid search within the frequency range $0.05f_c \lesssim f \leq f_{c2}$, where f_c is estimated from fitting Equation 15. In the fitting process using Equation 22, the fall-off rate in the middle frequency range is denoted as n_1, while n_2 represents the fall-off rate at high frequencies. Since individual spectra sometimes deviate from simple spectral functions, we fit Equation 22 exclusively to the stacked spectra, which represent the spherical average of all spectra over the focal sphere.

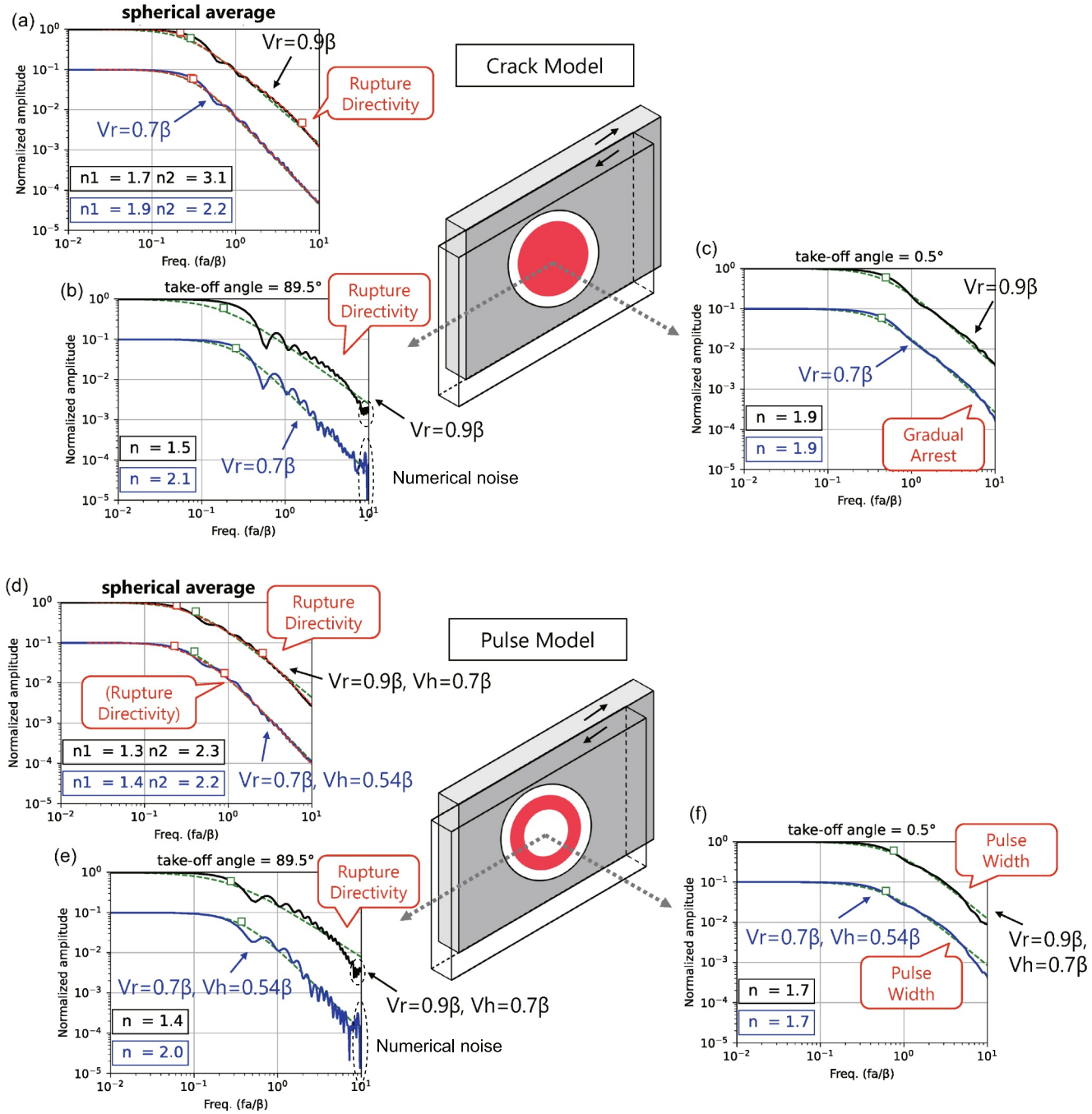

Figure 8. Far-field S-wave displacement spectra for (a–c) circular crack models and (d–f) circular pulse models. (a, d) Stacked spectra over the focal sphere. (b, e) Spectra at take-off angle = 89.5°. (c, f) Spectra at take-off angle = 0.5°. Black lines represent spectra for models with rupture speed $V_r = 0.9\beta$ and the blue ones are $V_r = 0.7\beta$. Spectra for the $V_r = 0.7\beta$ case are uniformly shifted vertically on the logarithmic axis for comparison. Green dashed lines indicate the best-fitting single-corner frequency model (Equation 15), while red dashed lines represent the best-fitting double-corner frequency model (Equation 22). Normalized corner frequencies f_c' and fall-off rates n are indicated. For the stacked spectra, intermediate- and high-frequency fall-off rates n_1 and n_2 are also indicated. Numerical noise in each spectrum, where present, is indicated by a dashed ellipse.

4.1. Circular Symmetrical Model

Figure 8 compares S-wave displacement spectra for circular symmetrical crack and pulse models with varying rupture speeds. The stacked S-wave spectra for the pulse model with $V_r = 0.9\beta$ exhibit a prominent second high-frequency corner (black line in Figure 8d). At large take-off angles ($\theta \approx 90^o$, i.e. along the fault plane), second

corners appear in both crack and pulse models with fast rupture speeds (black lines in Figures 8b and 8e), but are subtle or absent in models with slower rupture speeds (blue lines). The second corner at large take-off angles corresponds to the time from zero to the peak of the far-field displacement and is attributed to the rupture directivity effects (Figure 4).

To confirm this interpretation, we plot the distributions of displacement durations corresponding to the rising part, the falling part, and the total displacement duration, and superimpose them on the stacked spectra of the pulse model (Figure S4 in Supporting Information S1). The duration distribution peaks for the total duration and the rising portion approximately match the first (f_{c1}) and second (f_{c2}) corner frequencies, respectively, in the stacked spectra, suggesting that the second corner is associated with the rising part of the displacement.

Moreover, the subtle appearance of the second corner in the pulse model with a slower rupture speed (blue line in Figure 8e) indicates that this feature is not governed by the slip-pulse width. A slower rupture velocity reduces the rupture directivity effects and elongates the rising part of the displacement, resulting in a subtle second corner. Nevertheless, the rising part of the displacement still corresponds to the location of the second corner frequency (Figure S5 in Supporting Information S1), supporting our interpretation. The second corner in the stacked spectra primarily reflects the rupture directivity effects, because contributions from observation points along the fault plane dominate during spherical averaging. Furthermore, analytical solutions from Sato and Hirasawa (1973) for far-field displacements and spectra in crack models show that the mid-frequency spectrum dominates at large take-off angles, producing the second corner (Text S1 and Figure S6 in Supporting Information S1). This suggests an alternate explanation to interpreting the second corner in stacked spectra to slip-pulse width (e.g., Wang & Day, 2017), that is, that rupture directivity effects alone are sufficient to produce a second corner, even in spherically averaged stacked spectra.

At small take-off angles (normal to the fault plane), second corners appear in the pulse model across all rupture speeds (Figure 8f). This second corner corresponds to the time from the peak of the far-field displacement to zero, representing the duration of slip arrest after the rupture reaches the fault's edge. This duration depends directly on the slip-pulse width. Consequently, when comparing models with different rupture speeds V_r (i.e., different slip-pulse durations), the second corner shifts to higher frequencies in models with larger V_r (Figure 8f).

In the crack model, at small take-off angles, second corners are absent in the models with a fast rupture speed, whereas the model with a slow rupture speed exhibits second corners, albeit less pronounced (Figure 8c). The fall-off rate for the high-frequency range in the slow rupture speed model exceeds 2 and approaches 3 (indicated by a deviation from the blue curve from the green line in Figure 8c). In the model with a slower rupture speed, the time required for the shear stress to decrease from the rupture front to the dynamic shear strength τ_d becomes longer. Consequently, the model with a slower rupture speed results in a more gradual rupture termination at the fault's edge. As discussed in detail in Section 5, gradual rupture arrest produces a larger high-frequency fall-off rate, which, in turn, can create a second corner frequency.

Note that double-corner frequency spectra related to rupture directivity effects do not appear in the P-wave spectra, while those related to pulse width and gradual arrest appear similar to the S-wave spectra (Figure S7 in Supporting Information S1). The large difference between the sub-shear rupture speed and the P-wave speed significantly reduces the rupture directivity effects, elongates the rising part of the displacement (Figure S3 in Supporting Information S1), and shifts the second corner toward the first, resulting in a very subtle second corner in the stacked spectra (Figure S7 in Supporting Information S1). In essence, this situation is similar to the S-wave spectra with a slow rupture speed (blue line in Figure 8e). In addition, increasing the value of A_h slightly enhances the energy of the high-frequency portion of the spectra, but its overall effect is minimal, with only an up-to 5% impact on the corner frequency and fall-off rate (Figure S8 in Supporting Information S1).

To examine how stopping phases influence our interpretation of the second corner frequency, we consider an additional pulse model in which the rupture gradually slows down in a narrow $(0.2a)$ annular zone near the circular fault edge (Figure S9 in Supporting Information S1). While gradual rupture arrest leads to a steeper high-frequency fall-off compared to the case in Figure S4 in Supporting Information S1, the directivity effects illustrated in Figure 5 remain unchanged and thus have no significant influence on the location of the second corner. This result is also confirmed for the case of a slower rupture speed (Figure S10 in Supporting Information S1). These additional results suggest that the emergence of the second corner frequency in the stacked spectra arises from enhanced intermediate spectral amplitudes caused by the rupture directivity effects (Figure 4).

To assess the effect of the growing slip-pulse width on double-corner spectra, we also consider a model in which the rupture and healing speeds are identical, resulting in a constant slip-pulse width (though this model lacks self-similarity) (Figure S11 in Supporting Information S1). This alternative model initially behaves like a crack-like rupture, with the healing front beginning to propagate at the same speed as the rupture front after a certain time, eventually resulting in a pulse-like rupture. The emergence of double-corner frequency spectra in this model is consistent with that in our self-similar pulse model (Figure S11 in Supporting Information S1). This result confirms that the second corner in the stacked spectra of the circular symmetrical pulse model primarily caused by the rupture directivity effects is not specific to the self-similar nature of our model but rather reflects a more general feature of pulse-like ruptures.

4.2. Circular Asymmetrical Model

To examine whether double-corner frequency spectra emerge in asymmetrical rupture scenarios, we consider a source model where the rupture initiates at one end of a circular fault and propagates toward the opposite end (Figure 1c). Moment-rate functions for the asymmetrical rupture scenarios are shown in Figures S2c and S2d in Supporting Information S1. We compare the characteristics of displacement spectra between asymmetrical pulse and crack models. Figure 9 illustrates the far-field S-wave displacement spectra for these models. Similar to the symmetrical pulse model, the asymmetrical pulse model shows second corners in S-wave spectra at small take-off angles, albeit less distinctly, which are related to the slip-pulse width (Figure 9h). However, at large take-off angles, individual spectra in the asymmetrical pulse model do not display second corners (Figures 9f and 9g), while the stacked spectra reveal a clear second corner (Figure 9e).

The emergence of a second corner in the stacked S-wave spectra is attributed to a rupture directivity effect, not the slip-pulse width. In the rupture propagation direction, the far-field displacement begins when waves generated at the rupture initiation point reach the observation point and ends when waves from the slip pulse at the fault edge arrive. This results in a first corner frequency that reflects the duration of far-field displacement in the rupture propagation direction rather than the slip-pulse width. Consequently, the first corner frequency is particularly high at observation points in the rupture propagation direction (Figure 9f), especially for models with high rupture speeds (compare black and blue lines in Figure 9f), as expected.

Differences in the first corner frequencies in the rupture propagation direction (Figure 9f) and other directions (e.g., Figure 9g) give rise to the emergence of a second corner in the stacked spectra of the asymmetrical pulse model. In the mid-frequency range, the stacked spectra exhibit a fall-off rate of $\sim$1.5 (Figure 9e). This occurs because spectra in the relevant frequency range showing flat characteristics (fall-off rate $\sim$0) in the rupture propagation direction are combined with spectra exhibiting a fall-off rate of $\sim$2 in other directions. At frequencies exceeding the first corner frequency in the rupture propagation direction, the stacked spectra display a fall-off rate of $\sim$2, as this feature is consistent across spectra from all large take-off angles. Hence we attribute the second corner frequency in the stacked spectra of the asymmetrical pulse model to a rupture directivity effect. Although this directivity effect differs from that illustrated in Figure 4, it similarly arises from the directionality of rupture propagation and is thus also classified as a directivity effect.

In the asymmetrical crack model, the first corners in S-wave spectra in the rupture propagation direction are smaller than those in the pulse model (Figure 9b). This is because the absence of a self-healing front in the crack model allows slip to persist longer, resulting in an extended displacement duration. Consequently, the first corner frequencies in the rupture-propagation and opposite directions are closer together, making the second corner in the stacked spectra indistinguishable and resulting in single-corner stacked spectra.

Additionally, we examine the dependence of rupture speed on the first corner frequency in asymmetrical pulse models. The asymmetrical model demonstrates similar rupture speed dependence for normalized corner frequencies and fall-off rates as observed in the symmetrical models (Table 2).

4.3. Elliptical Symmetrical Source Model With Supershear Rupture

Earthquake rupture may propagate at supershear speeds. To investigate the effect of Mach waves on resulting spectra, we consider an elliptical pulse model with supershear rupture along the Mode II direction, following the approach of Kaneko and Shearer (2015) (Figure 1d). The ellipticity of the fault is quantified by its eccentricity ϵ, defined as

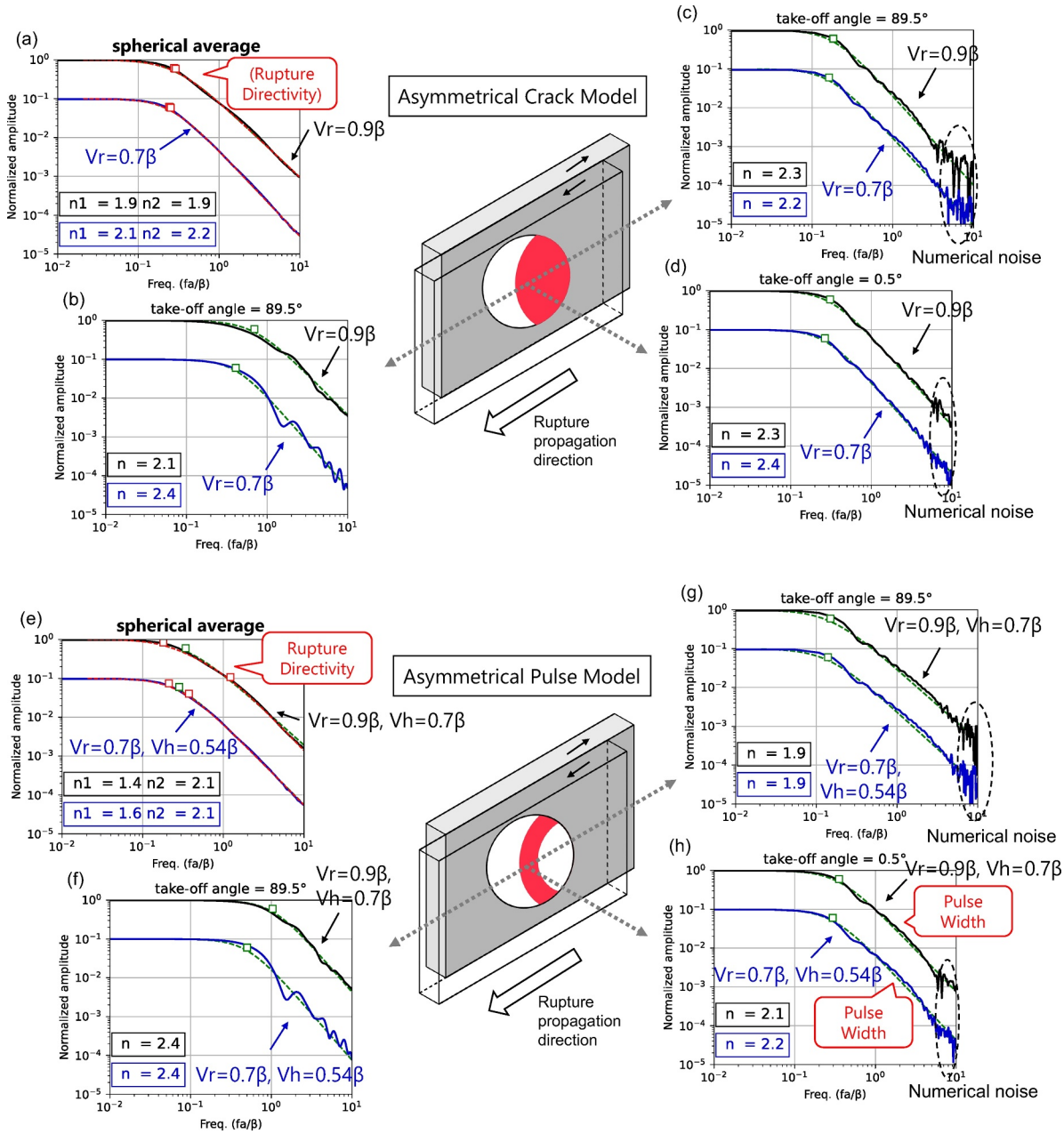

Figure 9. Far-field S-wave displacement spectra for (a–d) asymmetrical crack models and (e–h) asymmetrical pulse models. (a, e) Stacked spectra over the focal sphere. (b, f) Spectra at take-off angle = 89.5° in the direction of rupture propagation. (c, g) Spectra at take-off angle = 89.5° in the direction opposite to rupture propagation. (d, h) Spectra at take-off angle = 0.5°. Spectra for the $V_r = 0.7\beta$ case are uniformly shifted vertically on the logarithmic axis for comparison. Numerical noise in each spectrum, where present, is indicated by a dashed ellipse. The color scheme and indicated values follow those in Figure 8.

$$\epsilon = \sqrt{1 - \left(\frac{b}{a}\right)^2}, \tag{23}$$

where a and b are the major and minor axes, respectively. For $\epsilon = 0$, the fault is circular, whereas $0 < \epsilon < 1$ describes an elliptical fault. The rupture speed V_r and healing speed V_h can be expressed as

$$V_r = V_x V_y \left(\frac{x^2 + y^2}{V_y{}^2 x^2 + V_x{}^2 y^2} \right)^{1/2} \tag{24}$$

$$V_h = V_{hx} V_{hy} \left(\frac{x^2 + y^2}{V_{hy}{}^2 x^2 + V_{hx}{}^2 y^2} \right)^{1/2}, \tag{25}$$

where V_x and V_y are the rupture speeds, and V_{hx} and V_{hy} are the healing speeds along the major and minor axes, respectively. We adopt the same nondimensionalizations as Kaneko and Shearer (2015), and the source dimension a is replaced with $\sqrt{ab}$. The rupture propagates with a rupture front and healing front maintaining the elliptical fault shape. In the following, results are presented for a model with an eccentricity $\epsilon = 0.83$. Moment-rate functions for elliptical source scenarios are shown in Figures S2e in Supporting Information S1.

In the subshear rupture model, double-corner frequency spectra for S waves are evident at both small take-off angles (Figure 10c) and large take-off angles (Figure 10b). These double corners are caused by pulse width and rupture directivity, respectively. These features resemble the spectral characteristics observed in the circular symmetrical model. Notably, at large take-off angles, the double-corner frequency spectra are observed only in the direction of the fault's long axis. The second corner in the stacked spectra (Figure 10a) is less prominent because variability in the spectral shapes among stations with large take-off angles, caused by the fault's ellipticity and asymmetry, contributes to the stacked spectra. This suggests that the second corner in stacked spectra resulting from rupture directivity depends on fault symmetry.

The spectral characteristics of the supershear rupture model are similar to those of the subshear rupture model, with one exception (blue lines in Figures 10a–10d). At small take-off angles close to the fault normal direction, double-corner frequency spectra appear due to the pulse width (Figure 10c), while at large take-off angles, they result from rupture directivity (Figure 10b). However, the effect of shear Mach waves is evident. Shear Mach waves emerge at the "Mach angle" $\cos^{-1}(\beta/V_r)$ (e.g., Bernard & Baumont, 2005; Mello et al., 2010), which is 51.3° in this model. At this angle, prominent double-corner frequency spectra emerge due to the sharp rise of the far-field displacements (Figure 10d). The stacked spectra of the supershear rupture model include the effect of Mach waves, with the mid-frequency range showing larger amplitudes than in the subshear rupture model (Figure 10a).

Figures 10e–10g show the P-wave spectra for the symmetrical elliptical model under subshear and supershear rupture conditions. For subshear rupture (black line in Figure 10f), the second corner is absent, consistent with the circular symmetrical model. For supershear rupture (blue line in Figure 10f), the spectra exhibit a second corner attributed to P-wave rupture directivity, as the rupture speed approaches the medium's P-wave speed. Additionally, the second corner associated with the pulse width is evident in the P-wave spectra (Figure 10f). However, the effect of Mach waves is absent, as the rupture speed in this model remains below the P-wave speed.

4.4. Elliptical Asymmetrical Model

To further explore the emergence of a second corner frequency in stacked spectra under asymmetrical pulse scenarios, we consider a source model in which the rupture initiates at one end of an elliptical fault and propagates toward the opposite end (Figure 11). The ellipticity of the fault in this model is set to 0.94, and the moment-rate function is shown in Figure S2f in Supporting Information S1.

Due to the high ellipticity, which amplifies the effects of stopping phases from the fault edges and makes the rupture more pulse-like, the asymmetrical crack model exhibits behavior similar to that of the asymmetrical pulse model. Stacked spectra for both the crack and pulse models with $V_r = 0.9\beta$ display second corner frequencies (Figure 11a). This behavior is attributed to the rupture directivity effects, consistent with findings discussed in Section 4.2 for the circular asymmetrical model. Notably, second corner frequencies do not emerge in the spectra at individual observation stations (Figures 11b–11d). However, due to numerical noise, it remains unclear whether second corners are present at small take-off angles (Figure 11d). Overall, these results suggest that deviations from an idealized circular fault geometry introduce complexities that make the interpretation of second corner frequencies more challenging.

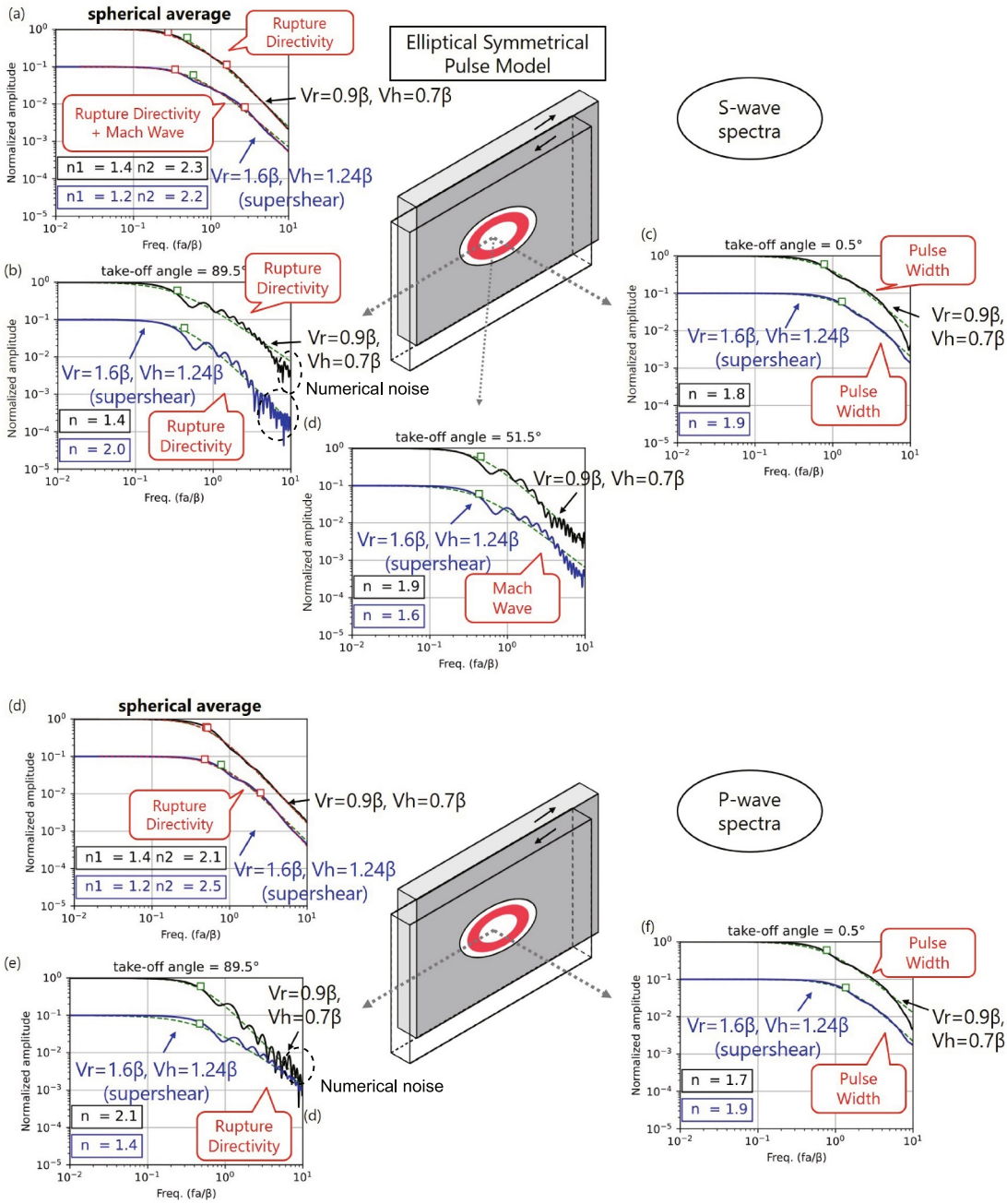

Figure 10. Far-field S-wave (a–d) and P-wave (e–g) displacement spectra for elliptical symmetrical pulse models. Black lines represent spectra for the model with rupture speed $V_r = 0.9\beta$ (subshear rupture speed), while blue lines correspond to $V_r = 1.6\beta$ (supershear rupture speed). Spectra for the $V_r = 1.6\beta$ case are uniformly shifted vertically on the logarithmic axis for comparison. (a, e) Stacked spectra. (b, f) Spectra at take-off angle = 89.5°. (c, g) Spectra at take-off angle = 0.5°. (d) Spectra at take-off angle = 51.5°, which corresponds to the "Mach angle". Numerical noise in each spectrum, where present, is indicated by a dashed ellipse. The color scheme and indicated values follow those in Figure 8.

5. Source Model With Spontaneous Rupture Arrest

To evaluate the applicability of our conclusions from previous sections to other idealized source scenarios, we consider an alternative source model with spontaneous rupture arrest, motivated by Ke et al. (2022). Their dynamic model, which incorporates non-uniform initial stress, successfully reproduces well-established source scaling relationships for small earthquakes, including seismic moment, stress drop, and breakdown energy (Ke et al., 2022). Here we investigate the spectral properties of this model, referred to as the "gradual arrest model."

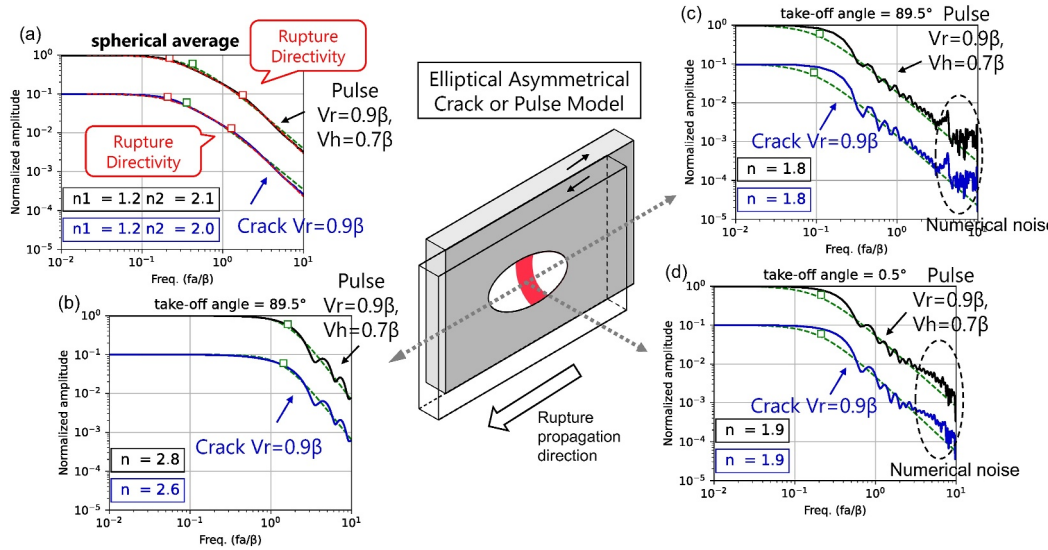

Figure 11. Far-field S-wave displacement spectra for elliptical asymmetrical pulse model (black lines) and elliptical asymmetrical crack model (blue lines) with rupture speed $V_r = 0.9\beta$. (a) Stacked spectra over the focal sphere. (b) Spectra at take-off angle = 89.5° in the direction of rupture propagation. (c) Spectra at take-off angle = 89.5° in the direction opposite to rupture propagation. (d) Spectra at take-off angle = 0.5°. Spectra for the crack model are uniformly shifted vertically on the logarithmic axis for comparison. Numerical noise in each spectrum, where present, is indicated by a dashed ellipse. The color scheme and indicated values follow those in Figure 8.

In the gradual arrest model, the initial shear stress τ_0, and thus the dynamic stress drop, decrease linearly from the center to the fault edge (Figures 12a and 12b). The initial stress distribution is adjusted so that the average dynamic stress drop is 4 MPa, matching that of the symmetrical circular crack model. Unlike previous models, the radius a is not fixed but defined as the distance enclosing the area where the final slip exceeds 5% of the maximum. In this model, rupture decays progressively outward from the center (Figure 12c). The final slip and stress-drop distributions are similar to those of the circular crack model but are more concentrated near the center and taper smoothly toward the edges (Figures 12d and 12e). Moment-rate functions for these models are shown in Figures S2g and S2h in Supporting Information S1.

The gradual arrest model yields distinct spectral properties. Figure 13 shows the spectral characteristics of gradual arrest, crack and pulse models. In both models, the mean fall-off rate approaches 3, significantly higher than in models where the rupture stops abruptly at the fault edge (Figures 13c and 13d). The gradual arrest eliminates the dominance of high-frequency components in the spectra, resulting in a steeper high-frequency fall-off. In particular, in models with low rupture velocity (blue lines in Figures 13a and 13b), the intermediate spectral slope has a fall-off rate near 2, while the high-frequency slope approaches 3 due to gradual rupture arrest. This is consistent with the findings of Madariaga (1977), who demonstrated that abrupt changes in rupture velocity (e.g., stopping phases) produce spectra with ω^{-2}-type high-frequency decay. In contrast, smoother changes in rupture velocity, as in the gradual arrest model, result in higher fall-off rates. Note that, with the diminishing high-frequency energy in these models, numerical noise in spectra becomes more apparent in the high-frequency components ($fa/\beta \sim 10$).

In models with high rupture velocity (black lines in Figures 13a and 13b), double-corner frequency spectra are clearly seen. While these spectral characteristics are consistent with the arresting pulse model described by Wang and Day (2017), we attribute the emergence of the second corners to a combination of gradual arrest and rupture directivity effects, not the slip-pulse width. Compared to the circular pulse model described in Section 4.1, the double-corner frequency spectra are more prominent in the gradual arrest model because the steep high-frequency fall-off enhances the distinction between the first and second corners (Figures 13a and 13b).

It is important to note that double corners in this model should not be interpreted as evidence of pulse-like rupture behavior. Instead, they reflect the effects of gradual rupture arrest. The steep fall-off rates observed in the gradual

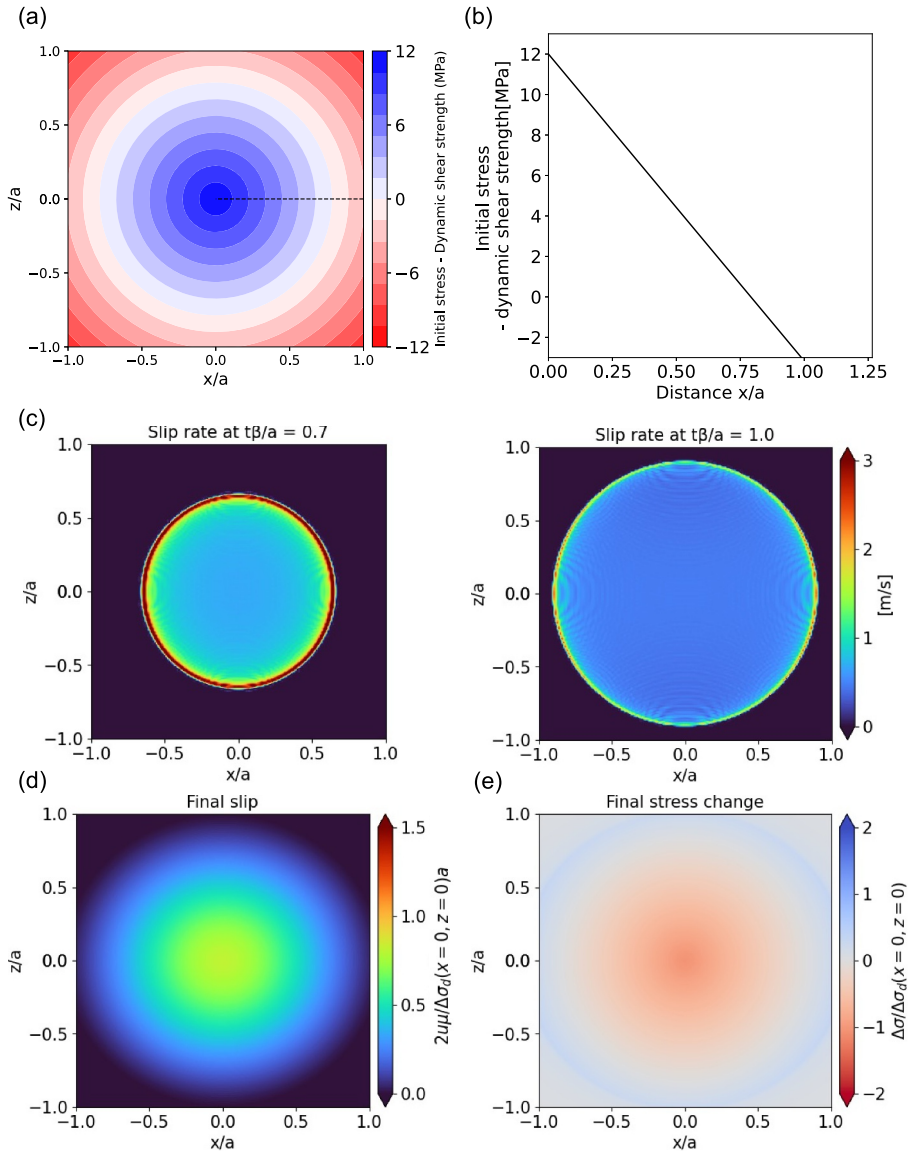

Figure 12. Source characteristics of the gradual arrest model. (a) Distribution of initial shear stress minus dynamic shear strength on the fault, decreasing with distance from the fault center. (b) Profile of initial shear stress minus dynamic shear strength along the dashed line in panel (a). (c) Snapshots of slip-rate evolution, illustrating spontaneous rupture arrest. (d) Final slip distribution, representing the rupture's spatial extent. (e) The distribution of shear stress change.

arrest model are uncommon and suggest that this model may not represent real earthquakes accurately. Hence, the applicability of gradual arrest models to natural seismic events is questionable.

6. Heterogeneous Source Model

The models considered so far are highly idealized compared to real earthquakes. Observational studies, such as those by Dreger et al. (2007), suggest that small earthquakes can exhibit very high stress drops, ranging from 66.7 to 93.9 MPa, and that prominent asperities can exist at small scales. To examine the role of stress and slip heterogeneities in earthquake spectra, we introduce a heterogeneous source model with spatially variable initial stress, generated using the method of Noda et al. (2013). In this model, the dynamic stress drop $\mathcal{R}$ (i.e., difference between the initial shear stress and the dynamic shear strength) is randomly distributed according to the following expression:

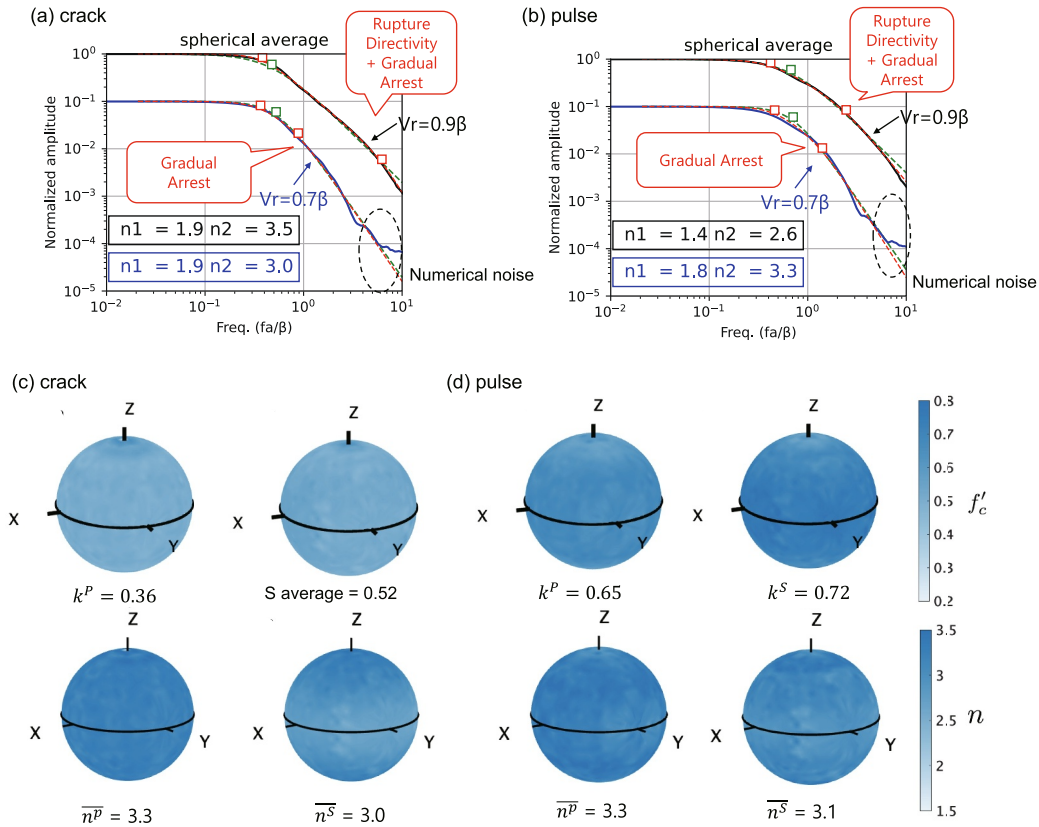

Figure 13. Far-field S-wave displacement spectra for the gradual arrest model with rupture speed $V_r = 0.7\beta$. Spherical averages of spectra for circular gradual arrest models, comparing (a) crack-like and (b) pulse-like rupture scenarios. Spectra for the $V_r = 0.7\beta$ case are uniformly shifted vertically on the logarithmic axis for comparison. (c, d) Variations of P- and S-wave normalized corner frequencies f_c' and fall-off rates n across the focal sphere, with the fault oriented along the X-Y plane. Numerical noise in each spectrum, where present, is indicated by a dashed ellipse. The spherical averages of high-frequency fall-off rates in the gradual arrest model are $n \sim 3$.

$$F[\mathcal{R} - 4\ \text{MPa}] = C_\chi H(q_{\text{tr}} - q)\, q^{-\frac{\nu+1}{2}} F[X], \tag{26}$$

where $F[\ \ ]$ is the discrete Fourier transform, X represents a standard normal random variable, q refers to the magnitude of a 2D wavenumber vector, $\nu + 1$ specifies the decay rate of the power spectral density of R with increasing q, H is the Heaviside step function, q_{tr} is the truncation wavenumber limiting the range of q, and C_χ is a constant chosen to ensure that the standard deviation of the distribution equals χ. The spatial average of $\mathcal{R}$ is set to 4 MPa, matching the dynamic stress drop $\Delta\tau_d$ in the previous circular models. We set $\nu = 1$ and the standard deviation $\chi = 6$ MPa.

Figure 14 illustrates the source and spectral characteristics of heterogeneous crack and pulse models, with the corresponding distribution of R shown in Figure S12a in Supporting Information S1. The stacked spectra for both models exhibit high-frequency fall-off rates of approximately 2.5 (Figure 14d). This relatively steep fall-off is attributed to gradual rupture arrest in regions with low initial stress before the rupture reaches the fault's edge. The heterogeneous models behave similarly to the gradual arrest model but with added complexity, leading to a higher fall-off rate that may not accurately represent realistic earthquake sources. At small take-off angles (0.5°), the pulse model shows the emergence of a second corner frequency due to the slip pulse width, while the crack model does not exhibit this feature (Figures 14e and 14f). This behavior is consistent with the spectra of circular source models without heterogeneities (Figures 8c and 8f).

To develop more realistic heterogeneous source models with sudden slip arrest and a ω^{-2}-type high-frequency spectral decay (e.g., Gallovič & Valentová, 2023), we modify the R distribution by assigning sufficiently small

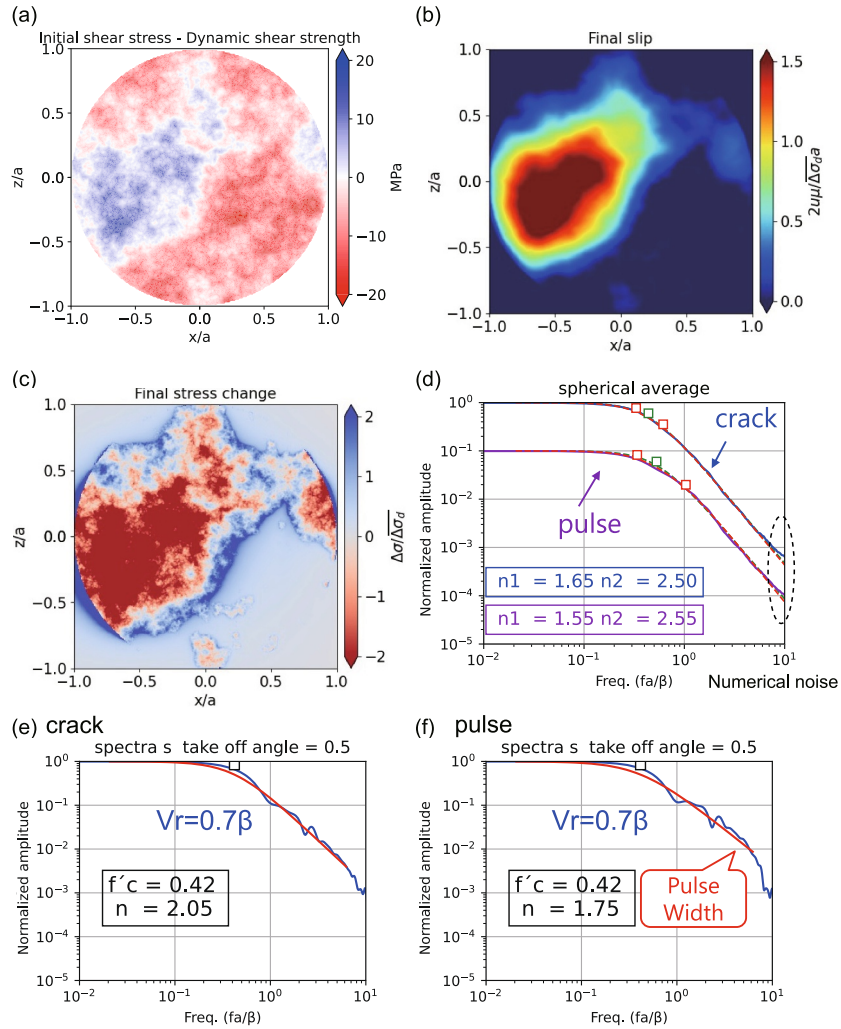

Figure 14. Source and spectral characteristics of crack and pulse models with stress heterogeneity. (a) Initial stress distributions on the fault. (b) Final slip distribution in the crack model. (c) Final stress change distribution in the crack model. (d) Stacked S-wave spectra for both the crack (blue) and pulse (purple) models. Green dashed lines indicate the best-fitting single-corner frequency model (Equation 15), and red dashed lines represent the best-fitting double-corner frequency model (Equation 22). Spectra for the pulse model are uniformly shifted vertically on the logarithmic axis for comparison. The high-frequency fall-off rate is elevated due to gradual arrest, though it remains lower than in the gradual arrest model. (e) S-wave spectra at a take-off angle = 0.5° in the crack model. The red line represents the best-fitting single-corner frequency model. (f) Spectra at take-off angle = 0.5° in the pulse model, showing the emergence of double-corner frequencies due to slip-pulse width. Numerical noise in each spectrum, where present, is indicated by a dashed ellipse.

negative values to regions where $\mathcal{R} < 4$ MPa (Figure S12b in Supporting Information S1), causing rupture cessation and no slip in those areas. Figure 15 shows results for two heterogeneous models with different random distributions. In the first model (Model A) (Figures 15a–15d), the heterogeneity is relatively simple, while the second model (Model B) (Figures 15e–15h) includes heterogeneities with a characteristic length scale related to the spatial width of the initial stress. Pronounced stopping phases due to spatially complex rupture arrest in both models result in pulse-like rupture behavior, and thus we focus on crack model results below. Examples of moment-rate functions in heterogeneous source models are shown in Figures S2i and S2j in Supporting Information S1.

Stacked spectra (Figures 15d and 15h) reveal a high-frequency fall-off rate approaching 2, consistent with abrupt slip arrest. The second corner frequency emerges in the stacked spectra of Model B (Figures 15e–15h) but is absent in Model A (Figures 15a–15d). Examination of 10 additional heterogeneous source models reveals that the

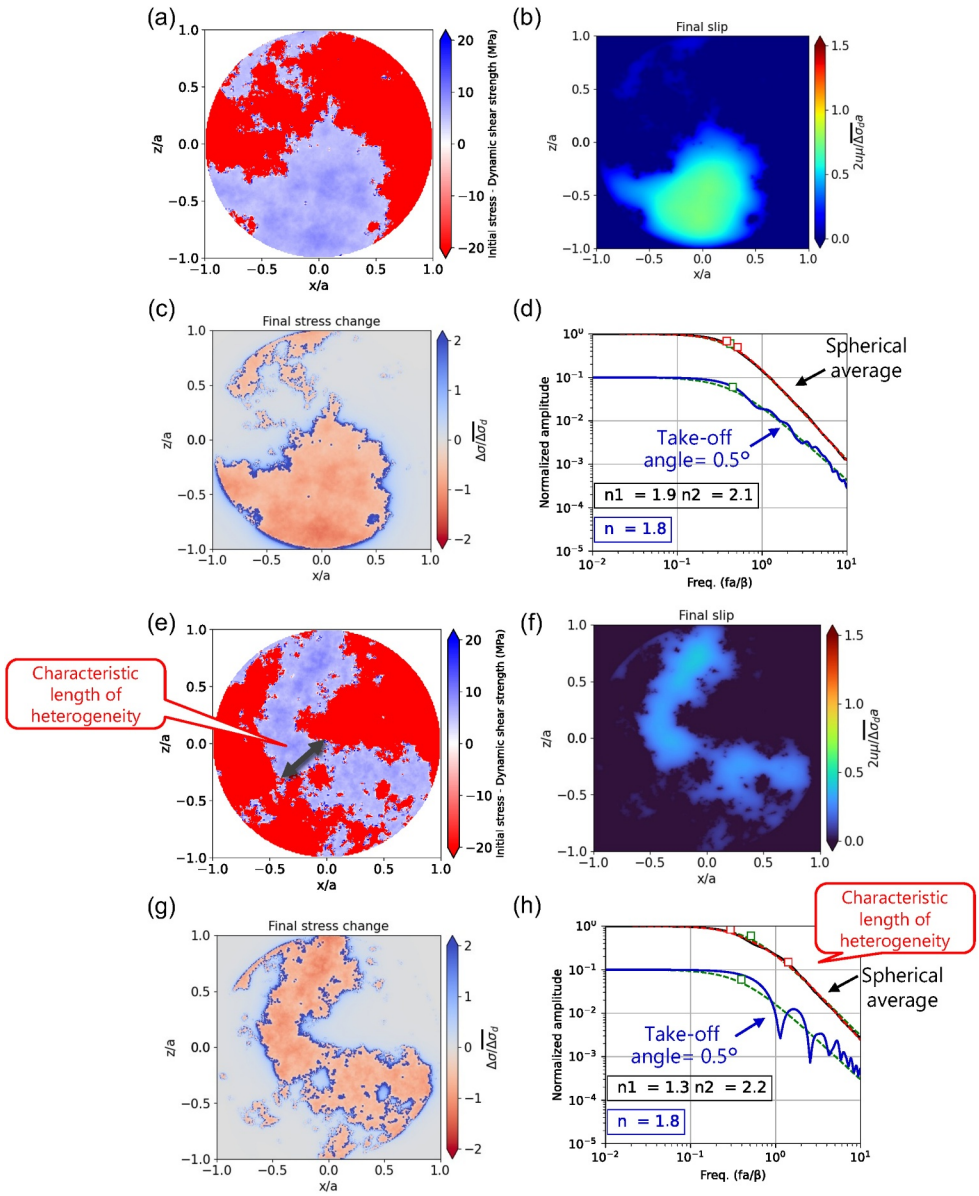

Figure 15. Source and spectral characteristics of two heterogeneous crack models: (a–d) Model A and (e–h) Model B with a characteristic length scale of heterogeneity related to the spatial width of the initial stress. (a, e) Initial stress distributions on the fault. (b, f) Final slip distributions. (c, g) Final stress change distributions. (d, h) Stacked S-wave spectra (black line) over the focal sphere and spectra at take-off angle = 0.5° (blue line). Spectra at the take-off angle = 0.5° are uniformly shifted vertically on the logarithmic axis for comparison. Spectra are fitted by the single-corner model (red lines) and the double-corner model (green lines), with the corresponding corner frequencies indicated.

second corner appears only when the heterogeneities have specific length scales related to the spatial width of the initial stress (e.g., Figure 15e). Notably, spectra at small take-off angles 0.5° do not exhibit second corners. These findings suggest that slip heterogeneity, defined by a scale-invariant power-law spectrum of initial stress, does not inherently produce a second corner. Even for pulse-like rupture due to slip and stress heterogeneities, the emergence of second corners is uncommon and depends on specific heterogeneity length scales. This highlights the potentially limited role of slip heterogeneity in the generation of double-corner frequency spectra, reinforcing the importance of rupture directivity and slip-pulse width in controlling spectral characteristics.

Second corner frequencies related to slip heterogeneities are also observed in the P-wave spectra. Figures S9b and S9d in Supporting Information S1 show the P-wave spectra of the heterogeneous models in Figures 15a and 15e,

Table 3
Summary of Key Factors Contributing to the Emergence of Double-Corner Spectra

Reason for S waves	Crack or pulse model	Change in fall-off rate (n) around f_{c2}	Observation point/location	Relevant figure
Slip-pulse width	pulse	1.5–2	Normal to the fault plane (small take-off angles)	Figures 8 and 10
Rupture directivity	both	1.5–2	Along the fault plane (large take-off angle)	Figures 8 and 11
Gradual rupture arrest	both	2–3	All directions (any take-off angle)	Figure 13
Characteristic length of slip heterogeneity	both	1.5–2	Along the fault plane (large take-off angle)	Figure 15
Mach waves (supershear rupture)	both	1.5–2	"Mach angle" (take-off angle ≃51°)	Figure 10
Reason for P waves	**Crack or pulse model**	**Change in fall-off rate (n) around f_{c2}**	**Observation point/location**	**Relevant figure**
Slip-pulse width	pulse	1.5–2	Normal to the fault plane (small take-off angle)	Figures 10 and S7 in Supporting Information S1
Rupture directivity for supershear event	both	1.5–2	Along the fault plane (large take-off angle)	Figure 10
Gradual rupture arrest	both	2–3	All directions (any take-off angle)	Not shown
Characteristic length of slip heterogeneity	both	1.5–2	Along the fault plane (large take-off angle)	Figure S13 in Supporting Information S1

respectively. Second corners are absent in both types of heterogeneity (Figures S9a and S9c in Supporting Information S1). Since the second corner is associated with the sharp rise in far-field displacements, the greater relative difference between the rupture speed and the P-wave speed results in a more gradual rise in the far-field displacements. To produce a model with a sharper rise of far-field P-wave displacements, we consider another heterogeneous model with a smaller characteristic length (Figure S13e in Supporting Information S1). In this model, with a rupture speed $V_r = 0.9\beta$, the sharper rise in far-field displacements leads to the appearance of second corners in the P-wave stacked spectra (Figure S13f in Supporting Information S1). Hence, second corners related to the characteristic length of slip heterogeneity appear not only in S-wave stacked spectra but also in P-wave stacked spectra.

7. Discussion

7.1. Why and Where Do Double-Corner Spectra Appear?

From the various models analyzed in the previous sections, we identify five main mechanisms responsible for the appearance of double-corner frequency spectra, which are summarized in Table 3:

1. Slip-pulse width.
2. Rupture directivity.
3. Gradual rupture arrest.
4. Characteristic length of slip heterogeneity.
5. Mach waves caused by supershear rupture.

Double-corner spectra associated with mechanism 4 (heterogeneity length scales), which can occur in both crack and pulse models (Section 6), resemble previously proposed models that incorporate asperities or multiple subevents (e.g., Atkinson & Silva, 2000; Boatwright, 1988; Boatwright & Choy, 1992; Luco, 1985). For crack

models with a rupture speed of ∼70% of the S-wave speed (and therefore a reduced rupture directivity effect), mechanisms 3 and 4 are the only processes that allow double-corner spectra to persist, although mechanism 3 yields a high-frequency fall-off rate approaching ∼3 (Table 3). For subshear crack- and pulse-like ruptures without heterogeneities, double-corner spectra produced by rupture directivity appear only in the S-wave spectra (Table 3). For supershear crack- and pulse-like ruptures, Mach waves can generate double-corner frequency spectra exclusively in the S-wave spectra (Table 3). Although one can construct heterogeneous source models with multiple crack-like subevents that yield shallow falloff rates or multiple corner frequencies (e.g., Boatwright, 1988; Luco, 1985), our focus here is on the relatively simple, smooth pulse-like ruptures examined in our numerical experiments.

Spectral characteristics of each mechanism are notably different (Table 3). For mechanisms (1), (2), (4), and (5) above, the middle-frequency range is pronounced, leading to a fall-off rate of approximately 1.5. The high-frequency fall-off rate of ∼2 results in the second corner frequency. In contrast, for mechanism (3) (gradual arrest), suppression of high-frequency radiation due to the absence of sharp stopping phases results in a fall-off rate approaching ∼3. Gradual arrest is an unlikely explanation for the emergence of double-corner frequency spectra in real earthquakes since the observed fall-off rates are generally closer to ∼2.

Observation locations also influence the emergence of double-corner frequency spectra (Table 3). For mechanism (1) (slip-pulse width), second corners appear at small take-off angles (normal to the fault plane), unaffected by rupture directivity. For mechanisms (2) (rupture directivity) and (4) (heterogeneity length scales), second corners emerge from steep displacement rises, observed at large take-off angles (along the fault plane). Second corners in S-wave spectra may arise at the observation sites corresponding to the Mach angle. For mechanism (3) (gradual arrest), second corners may be observed at all stations.

Stacked spectra over the entire focal sphere combine effects from various mechanisms, complicating the identification of specific causes for second corners. To detect second corners indicative of the slip-pulse width (mechanism 1), it is crucial to focus observations at small take-off angles (normal to the fault plane). Observing a change in the fall-off rate from ∼1.5 to ∼2 at such take-off angles may serve as evidence of pulse-like rupture behavior. However, second high-frequency corners directly linked to the slip-pulse width are absent in station-averaged or stacked spectra. This suggests that observational studies of natural earthquakes relying on such spectra would likely miss second corners associated with slip-pulse width. Therefore, observations spanning a range of take-off angles, from small to large, are essential for understanding the mechanisms behind the emergence of double-corner spectra.

S-wave spectra are inherently more complex than P-wave spectra, particularly due to rupture directivity effects in subshear ruptures. In contrast, second corners in P-wave spectra, where the fall-off rate changes from ∼1.5 to ∼2, are limited to mechanisms (1) (pulse width) and (4) (heterogeneity length scales). Hence, utilizing P-wave spectra may provide a more straightforward approach to interpreting double-corner frequency spectra and identify second corner frequencies related to the slip-pulse width.

Mechanisms (3) (gradual arrest), (4) (heterogeneity length scale), and (5) (Mach waves) operate only under specific circumstances. In particular, the infrequent appearance of second corner frequencies in pulse-like rupture models with slip and stress heterogeneity (Section 6) indicates that heterogeneity may have a more limited influence on generating double-corner spectra than previously suggested (e.g., Atkinson & Silva, 2000; Boatwright, 1988; Boatwright & Choy, 1992; Luco, 1985). Nevertheless, our models represent only certain types and spatial configurations of heterogeneity, which may differ from those occurring on natural faults, highlighting the need for further investigation.

Since second corners associated with the slip-pulse width (mechanism 1) are most clearly observed at small take-off angles, second corners reported for real earthquakes in recent studies may also reflect this mechanism. For example, Denolle and Shearer (2016) reported double-corner spectra in P waves recorded at small take-off angles from shallow-dipping thrust events, suggesting that the inferred second corners were controlled by the slip-pulse width. Similarly, second corners identified in California earthquake data sets dominated by near-vertical strike-slip events (Ji & Archuleta, 2020) likely include contributions from stations with small take-off angles (normal to the fault plane), where the maximum S-wave amplitude is expected. This source-receiver geometry enhances the spectral imprint of the slip-pulse width, implying that the inferred second corners primarily reflect this

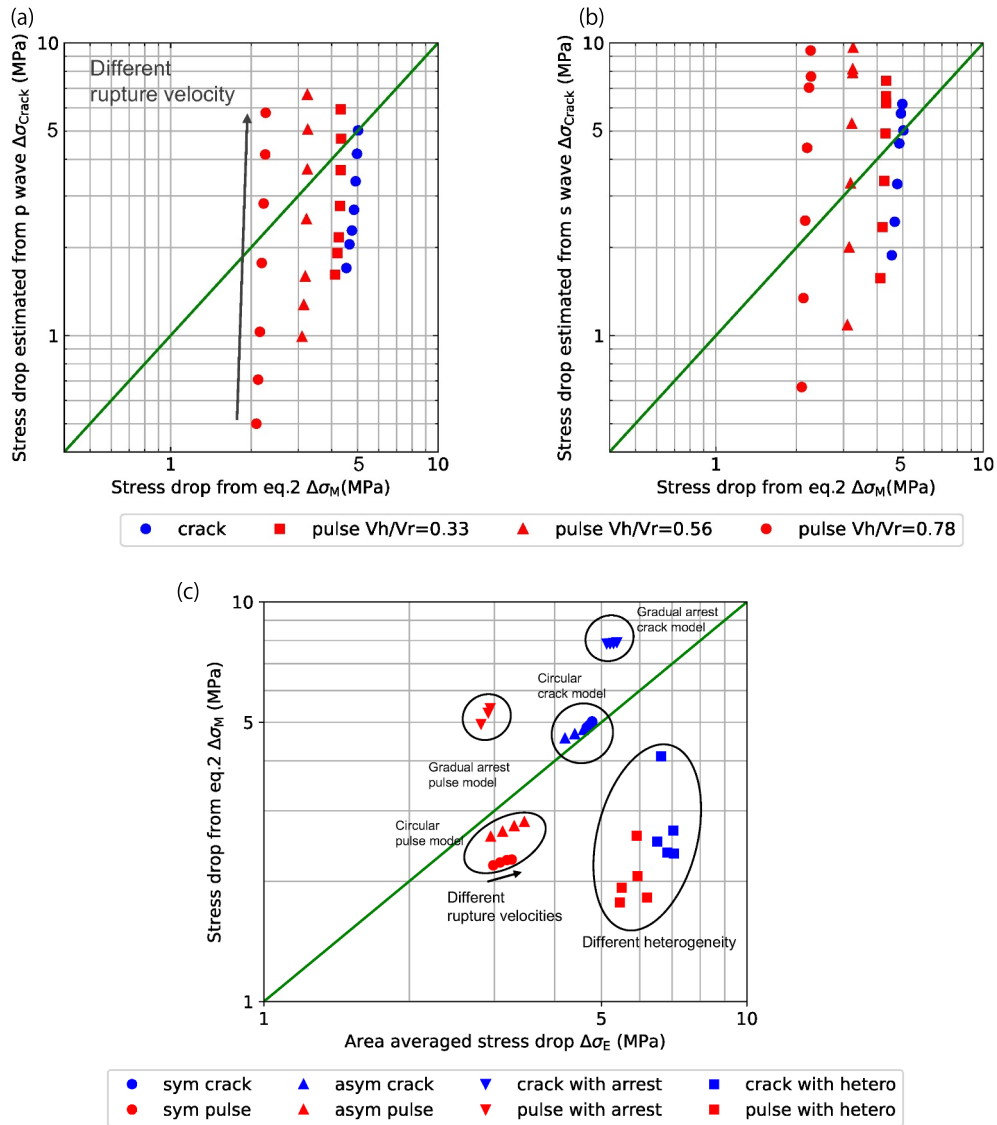

Figure 16. (a–b) Relationship between the moment-based stress drop, calculated using Equation 2, and the stress drop $\Delta\sigma_{crack}$ estimated from P- or S-wave spectral corner frequencies (Equation 4), assuming the symmetrical circular crack model with $k^P = 0.36$ and $k^S = 0.26$. Green lines indicate where the true stress drop equals the estimated stress drop. The pulse model shows greater variability in estimated stress drop. (c) Relationship between slip-weighted, area-averaged stress drop (true stress drop) and moment-based stress drop (estimated stress drop) across various models considered in this study. The green line denotes equality between true and estimated stress drops. Squares indicate heterogeneous models with varying levels of heterogeneity, while other symbols correspond to models with different rupture velocities.

mechanism. Such an interpretation is consistent with the inference by Ji and Archuleta (2020), who linked the second corner frequency to the average rise time.

7.2. Uncertainties in Estimated Stress Drop Arising From Crack Versus Pulse Model

To quantify uncertainties in stress drop estimation arising from unknown rupture speed and rupture mode, we report stress drop using three approaches: (a) Moment-based stress drop $(\Delta\sigma_M)$, which is calculated using Equation 2. (b) Estimated stress drop $(\Delta\sigma_{crack})$, which is calculated using k^P and k^S values from the crack model

with $V_r = 0.9\beta$. (c) Slip-weighted area-averaged stress drop ($\Delta\sigma_E$), which is weighted by the final slip distribution across the fault.

Figures 16a and 16b compare $\Delta\sigma_M$ with $\Delta\sigma_{crack}$ for the crack and pulse models. For the crack model with $V_r = 0.9\beta$, the two measures align, as expected. The variability in estimated stress drop due to unknown rupture speeds is larger in the pulse model than in the crack model (Figures 16a and 16b). The difference in rupture mode introduces overestimates of about a factor of 2.5 for P-wave estimates and a factor of more than 4 for S-wave estimates. The variability in stress drops estimated from the S wave of the pulse model is about twice as large as that of the crack model.

Figure 16c compares the moment-based stress drop $\Delta\sigma_M$ with the slip-weighted area-averaged stress drop $\Delta\sigma_E$, which reflects the 'true' stress drop. The plot of the symmetrical crack model lies almost on the green line, with a difference within 5%, as expected. This slight difference arises because the crack model in this study has a non-uniform stress drop. In the symmetrical and asymmetrical pulse models, the stress drop calculated using Equation 2, which is based on the assumption of the crack model, is smaller than the area-averaged stress drop weighted by the final slip calculated from the model (Figure 16c). This difference in stress drop is about 40% in the symmetrical pulse model with a rupture speed $V_r = 0.9\beta$ (Figure 16c). This is because smaller slip, caused by a self-healing pulse, leads to an underestimation of the moment-based stress drop $\Delta\sigma_M$.

In the gradual arrest model, the moment-based stress drop $\Delta\sigma_M$ is smaller due to the large, concentrated slip in the center of the fault (Figure 16c). Moment-based stress drops $\Delta\sigma_M$ in heterogeneous models appear to be underestimated by a factor of about 2–4 (Figure 16c). This result for the heterogeneous model aligns with the findings of Noda et al. (2013). The large underestimation occurs because the model captures an actual slip area smaller than the circular fault area in the heterogeneous model. Overall, these results suggest that unknown rupture modes, slip heterogeneities, and rupture arrest mechanisms may induce large scatter in estimated stress drops, almost independent of the actual stress drops.

Another important implication of our findings is that stacked spectra may not be entirely independent of directivity or radiation effects. Previous observational studies (e.g., Prieto et al., 2004; Shearer et al., 2006) suggested that stacked spectra provide a more accurate depiction of the average source spectrum and enable more robust estimates of source duration by reducing spectral distortions arising from source complexity and rupture propagation, when compared with spectra from individual stations. Our results demonstrate that directivity effects can persist in stacked spectra even for idealized, symmetric circular sources. Consequently, the first or second spectral corner identified in stacked spectra may reflect unavoidable source-radiation effects rather than purely intrinsic source characteristics, potentially biasing estimates of corner frequency and, in turn, stress drop.

7.3. Evidence of Pulse-Like Ruptures From Source Properties of Small to Moderate Size Earthquakes

To investigate whether small to moderate earthquakes follow pulse-like rupture modes, we compare source characteristics derived from our models with those inferred from the observational study of Yoshida and Kanamori (2023). Yoshida and Kanamori (2023) analyzed the source complexities and radiated energies of M_w 3–7 crustal earthquakes using high-quality seismic waveform data from approximately 1,700 events in Japan. Various source properties, including corner frequency, duration, seismic moment, radiated energy, and the Radiated Energy Enhancement Factor (REEF), were estimated. The REEF, a measure of source complexity, is defined as follows (Ye et al., 2018):

$$\mathrm{REEF} = \frac{E_R}{E_{R_{min}}} = \frac{5\pi\rho\beta^5}{6}\left(\frac{E_R}{M_0}\right)\left(\frac{T^3}{M_0}\right), \tag{27}$$

where $E_{R_{min}}$ represents the minimum radiated energy for a given seismic moment M_0 and source duration T (Kanamori & Rivera, 2004).

We aim to compare the relationship between corner frequency and scaled energy observed by Yoshida and Kanamori (2023) with predictions from our models. Our analysis focuses on events with $M_w < 5.5$, which were estimated using velocity seismograms and account for more than 98% of the events analyzed by Yoshida and Kanamori (2023) (Figure S14a in Supporting Information S1). Since Yoshida and Kanamori (2023) did not report estimated source dimensions for the events, we calculate normalized corner frequency to enable comparisons

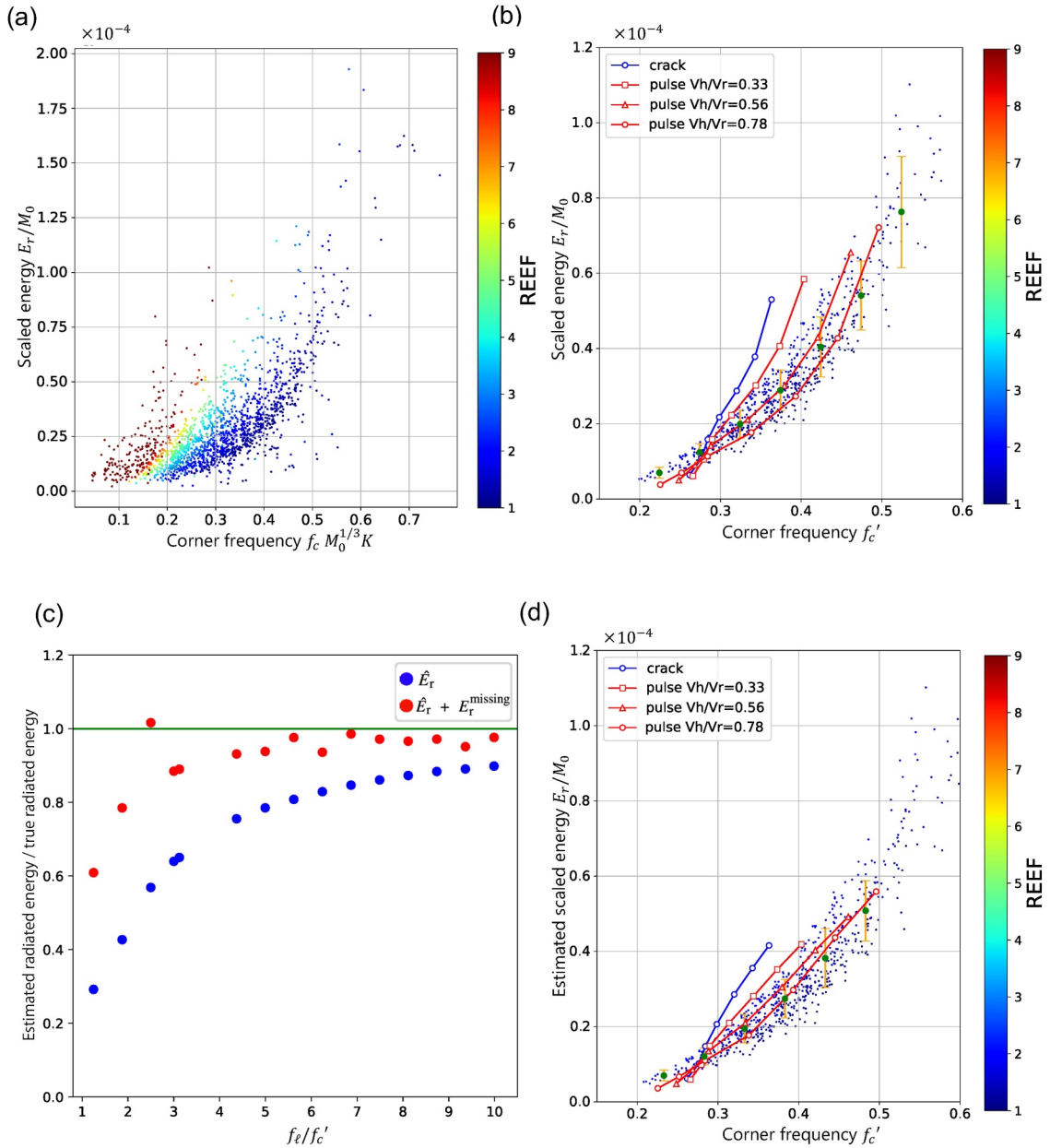

Figure 17. Relationship between normalized corner frequency and scaled energy for M_w 3–7 crustal earthquakes in Japan (Yoshida & Kanamori, 2023). (a) Results for ~1,500 events, with colors indicating the radiated energy enhancement factor (REEF). (b) Model-observation comparison, considering only data with REEF ≤2 and depths ≤15 km. Green markers denote average scaled energy at specific corner frequencies, with orange error bars indicating variance. Blue and red lines represent models' true scaled energy, with different rupture velocities. (c) Estimated radiated energy from ω^{-2} high-frequency extrapolation versus true radiated energy in the pulse model with $V_r = 0.9\beta$ and $V_h/V_r = 0.78$ as a function of cut-off frequency f_ℓ/f_c. Red and blue dots represent estimated radiated energy with $\left(\hat{E}_r + E_r^{missing}\right)$ and without extrapolation $\left(\hat{E}_r\right)$, respectively. (d) Normalized corner frequency versus estimated scaled energy with ω^{-2} high-frequency extrapolations applied to the models (see text). Pulse models with $V_h/V_r = 0.56$–0.78 fit the data, suggesting pulse-like rupture behavior in most small- to moderate-size earthquakes.

across different earthquake magnitudes. Assuming the source geometries of these events are circular and that their stress drops are constant and independent of magnitude:

$$\frac{{M_0}^2}{S^3} = \text{const} = c, \tag{28}$$

where $S = \pi a^2$ is the source area. By substituting a into Equation 16, the normalized corner frequency is expressed as:

$$f_c' = f_c \frac{a}{\beta} = f_c M_0{}^{1/3} K, \tag{29}$$

where

$$K = \frac{1}{c^{1/6}\pi^{1/2}\beta}. \tag{30}$$

We select an optimal constant $K = 1.2 \times 10^{-6}$ s/(N · m)$^{1/3}$ to match the results from our crack and pulse models.

Figures 17a and 17b illustrate the relationship between normalized corner frequency and scaled energy from Yoshida and Kanamori (2023), alongside our model predictions. In Figure 17a, all events from the observational data set are plotted, revealing an overall increasing trend in scaled energy with normalized corner frequency, particularly for events with small REEF values. Since our circular symmetrical crack and pulse models produce REEF values between 1 and 2, we focus exclusively on low-complexity events with REEF <2 and depths shallower than 15 km (Figure S14b in Supporting Information S1). Figure 17b compares the selected observational data with predictions from our circular symmetrical crack and pulse models. The pulse model results, especially those with V_h/V_r values between 0.56 and 0.78, align well with the observational data. This agreement suggests that the increase in scaled energy with rupture speed, as predicted by the pulse model, more closely matches the observed trend. In contrast, varying K in the crack model does not reproduce the observed relationship between normalized corner frequency and scaled energy.

A potential concern is whether Figure 17b presents a valid comparison between the model and data, as Yoshida and Kanamori (2023) estimated radiated energy by summing band-limited radiated energy, $\hat{E}_r$, with the missing high-frequency energy, E_r^{missing}, which was assumed to follow an ω^{-2}-source model. To address this issue, we further examine the potential bias introduced by this procedure. The radiated energy, E_r, estimated from far-field waves in the frequency domain for frequencies up to a cutoff frequency f_ℓ, is given by (e.g., Haskell, 1964):

$$\hat{E}_r = E_r^p + E_r^s = 2\rho \int_\Gamma \int_0^{f_\ell} \left[\alpha \left(\dot{u}^p \right)^2 + \beta \left(\dot{u}^s \right)^2 \right] df \, d\Gamma \approx 2\rho \int_\Gamma \int_0^{f_\ell} \beta \left(\dot{u}^s \right)^2 df \, d\Gamma, \tag{31}$$

where ρ is the density, $\dot{u}^p$ and $\dot{u}^s$ are far-field particle velocities for P and S waves, respectively, and Γ is the area over the focal sphere. Assuming an ω^{-2} high-frequency decay for $f \geq f_\ell$, the missing energy, E_r^{missing}, can be expressed as

$$E_r^{\text{missing}} = \frac{4\pi a_\ell^2 f_\ell^3}{5\rho\beta^5}, \tag{32}$$

where a_ℓ represents the spectral amplitude at $f = f_\ell$. The estimated total radiated energy, including the extrapolation, is then given by $E_r = \hat{E}_r + E_r^{\text{missing}}$ (Yoshida & Kanamori, 2023).

Figure 17c illustrates the extrapolation error, defined as the discrepancy between the estimated radiated energy using ω^{-2} high-frequency extrapolation and the true radiated energy, as a function of cutoff frequency f_ℓ for the pulse model with $V_r = 0.9\beta$ and $V_h/V_r = 0.78$. As expected, the accuracy of the estimated radiated energy deteriorates with smaller f_ℓ. However, the estimated total radiated energy, incorporating the extrapolation, agrees more closely with the true radiated energy. The estimated total energy consistently slightly underestimates the true energy, due to the directivity effect, which leads to an approximate $\omega^{-1.5}$ high-frequency decay in the intermediate frequency range (Section 4.1).

Figure 17d compares the scaled energy reported by Yoshida and Kanamori (2023) with the estimated scaled energy from the source models, incorporating ω^{-2} high-frequency extrapolations. For each model, the cutoff frequency f_ℓ is defined as

$$f_\ell(M_0) = k\beta\left(\frac{16}{7}\Delta\sigma_c\right)^{1/3} M_0^{-1/3}, \tag{33}$$

where $k = 0.37$, and $\Delta\sigma_c$, the scaling stress parameter, is set to 100 MPa, following Yoshida and Kanamori (2023). The agreement between the pulse models with $V_h/V_r = 0.78$ and the data in Figure 17d shows a slight improvement over Figure 17b. This improvement arises because the estimated radiated energy for the pulse models at faster rupture velocities is slightly smaller than the true radiated energy (Figure 17c), leading to a better match with the data. These results suggest that extrapolation errors have minimal impact, at least for the source models considered. Overall, based on the fit to the scaled energy, these findings indicate that most small- to moderate-size earthquakes with REEF <2 may be characterized by pulse-like rupture behavior.

Although the above inference is robust within the context of the adopted data set, it relies on source parameters estimated in a single study (Yoshida & Kanamori, 2023). Recent studies (Abercrombie & Baltay, 2025; Cochran et al., 2024) have reported substantial discrepancies in estimated source parameters resulting from different assumptions and analysis methods. Therefore, comparisons of our model predictions with source parameters derived using alternative approaches and from different regions will be necessary to further validate these findings.

7.4. Self-Similar Versus Non-Self-Similar Pulse-Like Ruptures

In this study, we assume that slip-pulse width increases as the rupture propagates, which is a plausible condition if earthquakes of all sizes are characterized by pulse-like rupture. Whether the slip-pulse width scales linearly with rupture size, as assumed here, or follows a more complex relationship (e.g., Gabriel et al., 2024) remains an open question. Although the self-similar pulse model developed in this study may not fully represent real earthquakes, it provides the first comprehensive analysis of such a model and its associated spectral characteristics. Further studies are needed to validate the assumption of self-similar scaling of slip-pulse width.

8. Conclusions

We developed fundamental models of earthquake rupture characterized by self-similar, self-healing slip pulses. We investigated the spectral characteristics and source properties of crack-like and pulse-like earthquake rupture models across various idealized and heterogeneous scenarios. By analyzing the far-field seismic spectra, we examined the conditions under which double-corner frequency spectra emerge and explored their implications for understanding earthquake rupture dynamics.

We identified five primary mechanisms responsible for the emergence of double-corner frequency spectra: (a) slip-pulse width, (b) rupture directivity, (c) gradual rupture arrest, (d) characteristic length of slip heterogeneity, and (e) Mach waves associated with supershear rupture. Spectra related to slip-pulse width are most prominent at small take-off angles from the fault normal, while those associated with rupture directivity and the characteristic length of slip heterogeneity are more evident at large take-off angles. Second high-frequency corners directly linked to slip-pulse width are primarily observed at receivers with small take-off angles (i.e., normal to the fault) and are generally absent in station-averaged or stacked spectra, suggesting their rarity in observational studies of natural earthquakes relying on such spectra.

Estimated stress drops strongly depend on the unknown rupture mode and rupture speed. In pulse-like models, the variability in estimated stress drops due to unknown rupture speeds is significantly larger than that in crack models. The self-healing nature of pulse-like ruptures introduces a systematic underestimation of moment-based stress drops, which can differ by up to 40% from slip-weighted area-averaged stress drops. Furthermore, heterogeneous and gradual arrest models amplify these uncertainties, complicating the interpretation of stress drops in real earthquakes.

By comparing our source models with observational data from Yoshida and Kanamori (2023), we found that the observed relationship between normalized corner frequency and scaled energy aligns more closely with pulse-like rupture models than with crack models. This finding suggests that most small- to moderate-size earthquakes may exhibit pulse-like rupture behavior, highlighting the importance of pulse-like earthquake models for interpreting such events.

The characteristic length of slip heterogeneity and gradual rupture arrest mechanisms lead to high-frequency spectral characteristics that deviate from those of idealized models. While these effects can produce double-corner frequency spectra under specific conditions, their role in representing realistic earthquake processes appears limited. Observations of double-corner frequency spectra in P-wave and S-wave data may instead reflect the presence of pulse-like ruptures, as suggested by observational studies of shallow crustal earthquakes.

This study highlights the importance of incorporating self-similar pulse-like rupture processes into earthquake source modeling and interpretation. Our results point out challenges in interpreting seismic source spectra and estimating source parameters such as stress drops, especially when rupture speeds and modes are uncertain. Future work should focus on further validating these findings through detailed observational analyses of small and moderate earthquakes, with particular emphasis on spectral features that may reveal pulse-like rupture behavior.

Conflict of Interest

The authors declare no conflicts of interest relevant to this study.

Data Availability Statement

The computer code used in this study is available at https://github.com/SPECFEM/specfem3d. Numerical data used to produce all the figures are available at Kano et al. (2025).

Acknowledgments
We thank Editor Rachel Abercrombie, the anonymous Associate Editor, František Gallovič, and two anonymous reviewers for their constructive comments, which helped improve the manuscript. We also thank Jesse Kearse, Keiko Kuge, Makiko Ohtani, and Bogdan Enescu for their suggestions, which helped to enhance the clarify of the manuscript. In addition, we thank Hiroyuki Noda for providing matlab scripts to generate heterogeneous distributions, and Keisuke Yoshida for providing us the source parameters of earthquakes in Japan. This study was supported by JSPS KAKENHI (23K03547, 21H05206), and ERI JURP 2024-S-B103 and 2024-S-B301 in Earthquake Research Institute, the University of Tokyo.

References

Abercrombie, R. E. (1995). Earthquake source scaling relationships from -1 to 5 M using seismograms recorded at 2.5-km depth. *Journal of Geophysical Research*, *100*(B12), 24015–24036. https://doi.org/10.1029/95JB02397

Abercrombie, R. E. (2014). Stress drops of repeating earthquakes on the San Andreas Fault at Parkfield. *Geophysical Research Letters*, *41*(24), 8784–8791. https://doi.org/10.1002/2014GL062079

Abercrombie, R. E. (2015). Investigating uncertainties in empirical Green's function analysis of earthquake source parameters. *Journal of Geophysical Research: Solid Earth*, *120*(6), 4263–4277. https://doi.org/10.1002/2015JB011984

Abercrombie, R. E. (2021). Resolution and uncertainties in estimates of earthquake stress drop and energy release. *Philosophical Transactions of the Royal Society A: Mathematical, Physical and Engineering Sciences*, *379*(2196), 20200131. https://doi.org/10.1098/rsta.2020.0131

Abercrombie, R. E., & Baltay, A. S. (2025). Magnitude, depth, and methodological variations of spectral stress drop within the SCEC/USGS community stress drop validation study using the 2019 ridgecrest earthquake sequence. *Bulletin of the Seismological Society of America*, *115*(6), 2741–2768. https://doi.org/10.1785/0120250056

Aki, K., & Richards, P. G. (2002). *Quantitative seismology* (2nd ed.). University Science Books, Sausalito, Calif.

Allmann, B. P., & Shearer, P. M. (2009). Global variations of stress drop for moderate to large earthquakes. *Journal of Geophysical Research*, *114*(B1), B01310. https://doi.org/10.1029/2008JB005821

Archuleta, R. J., & Ji, C. (2016). Moment rate scaling for earthquakes 3.3 ≤ M ≤ 5.3 with implications for stress drop. *Geophysical Research Letters*, *43*(23), 12004–12011. https://doi.org/10.1002/2016gl071433

Atkinson, G. M. (1993). Earthquake source spectra in eastern North America. *Bulletin of the Seismological Society of America*, *83*(6), 1778–1798.

Atkinson, G. M., & Silva, W. (1997). An empirical study of earthquake source spectra for California earthquakes. *Bulletin of the Seismological Society of America*, *87*(1), 97–113. https://doi.org/10.1785/bssa0870010097

Atkinson, G. M., & Silva, W. (2000). Stochastic modeling of California ground motions. *Bulletin of the Seismological Society of America*, *90*(2), 255–274. https://doi.org/10.1785/0119990064

Baltay, A., Abercrombie, R. E., Oth, A., & Uchide, T. (2025). Introduction to the special section on improving measurements of earthquake source parameters. *Bulletin of the Seismological Society of America*, *115*(3), 723–733. https://doi.org/10.1785/0120250055

Baltay, A., Ide, S., Prieto, G., & Beroza, G. (2011). Variability in earthquake stress drop and apparent stress. *Geophysical Research Letters*, *38*(6), L06303. https://doi.org/10.1029/2011GL046698

Bernard, P., & Baumont, D. (2005). Shear Mach wave characterization for kinematic fault rupture models with constant supershear rupture velocity. *Geophysical Journal International*, *162*(2), 431–447. https://doi.org/10.1111/j.1365-246X.2005.02611.x

Bernard, P., Herrero, A., & Berge, C. (1996). Modeling directivity of heterogeneous earthquake ruptures. *Bulletin of the Seismological Society of America*, *86*(4), 1149–1160. https://doi.org/10.1785/bssa0860041149

Boatwright, J. (1988). The seismic radiation from composite models of faulting. *Bulletin of the Seismological Society of America*, *78*(2), 489–508.

Boatwright, J., & Choy, G. L. (1992). Acceleration source spectra anticipated for large earthquakes in northeastern North America. *Bulletin of the Seismological Society of America*, *82*(2), 660–682.

Boore, D. M., Di Alessandro, C., & Abrahamson, N. A. (2014). A generalization of the double-corner-frequency source spectral model and its use in the SCEC BBP validation exercise. *Bulletin of the Seismological Society of America*, *104*(5), 2387–2398. https://doi.org/10.1785/0120140138

Brune, J. N. (1970). Tectonic stress and the spectra of seismic shear waves from earthquakes. *Journal of Geophysical Research*, *75*(26), 4997–5009. https://doi.org/10.1029/JB075i026p04997

Calderoni, G., & Abercrombie, R. E. (2023). Investigating spectral estimates of stress drop for small to moderate earthquakes with heterogeneous slip distribution: Examples from the 201620132017 amatrice earthquake sequence. *Journal of Geophysical Research: Solid Earth*, *128*(6), e2022JB025022. https://doi.org/10.1029/2022JB025022

Cochran, E. S., Baltay, A., Chu, S., Abercrombie, R. E., Bindi, D., Chen, X., et al. (2024). SCEC/USGS community stress-drop validation study: How spectral fitting approaches influence measured source parameters. *Bulletin of the Seismological Society of America*, *115*(3), 760–776. https://doi.org/10.1785/0120240140

Day, S. M. (1982). Three-dimensional finite difference simulation of fault dynamics: Rectangular faults with fixed rupture velocity. *Bulletin of the Seismological Society of America*, *72*, 705–727.

Denolle, M. A., & Shearer, P. M. (2016). New perspectives on self-similarity for shallow thrust earthquakes. *Journal of Geophysical Research: Solid Earth*, *121*(9), 6533–6565. https://doi.org/10.1002/2016JB013105

Dreger, D., Nadeau, R. M., & Chung, A. (2007). Repeating earthquake finite source models: Strong asperities revealed on the San Andreas Fault. *Geophysical Research Letters*, *34*(23), L23302. https://doi.org/10.1029/2007GL031353

Eshelby, J. D. (1957). The determination of the elastic field of an ellipsoidal inclusion, and related problems. *Proceedings of the Royal Society of London A*, *241*(1226), 3762013396. https://doi.org/10.1002/2016JB013105

Gabriel, A. A., Garagash, D. I., Palgunadi, K. H., & Mai, P. M. (2024). Fault size-dependent fracture energy explains multiscale seismicity and cascading earthquakes. *Science*, *385*(6707), eadj9587. https://doi.org/10.1126/science.adj9587

Gallovič, F., & Valentová, L. (2023). Broadband strong ground motion modeling using planar dynamic rupture with fractal parameters. *Journal of Geophysical Research: Solid Earth*, *128*(6), e2023JB026506. https://doi.org/10.1029/2023jb026506

García, D., Singh, S. K., Herráiz, M., Pacheco, J. F., & Ordaz, M. (2004). Inslab earthquakes of central Mexico: Q, source spectra, and stress drop. *Bulletin of the Seismological Society of America*, *94*(3), 789–802. https://doi.org/10.1785/0120030125

Gusev, A. (2013). High-frequency radiation from an earthquake fault: A review and a hypothesis of fractal rupture front geometry. *Pure and Applied Geophysics*, *170*(1), 65–93. https://doi.org/10.1007/s00024-012-0455-y

Harris, R. A., Barall, M., Andrews, D. J., Duan, B., Ma, S., Dunham, E. M., et al. (2011). Verifying a computational method for predicting extreme ground motion. *Seismological Research Letters*, *82*(5), 638–644. https://doi.org/10.1785/gssrl.82.5.638

Harris, R. A., Barall, M., Archuleta, R., Dunham, E., Aagaard, B., Ampuero, J. P., et al. (2009). The SCEC/USGS dynamic earthquake rupture code verification exercise. *Seismological Research Letters*, *80*(1), 119–126. https://doi.org/10.1785/gssrl.80.1.119

Haskell, N. A. (1964). Total energy and energy spectral density of elastic wave radiation from propagating faults. *Bulletin of the Seismological Society of America*, *54*(6A), 1811–1841. https://doi.org/10.1785/BSSA05406A1811

Heaton, T. H. (1990). Evidence for and implications of self-healing pulses of slip in earthquake rupture. *Physics of the Earth and Planetary Interiors*, *64*(1), 1–20. https://doi.org/10.1016/0031-9201(90)90002-F

Huang, Y., & Ampuero, J.-P. (2011). Pulse-like ruptures induced by low-velocity fault zones. *Journal of Geophysical Research*, *116*(B12), B12307. https://doi.org/10.1029/2011jb008684

Huang, Y., Ellsworth, W. L., & Beroza, G. C. (2017). Stress drops of induced and tectonic earthquakes in the central United States are indistinguishable. *Science Advances*, *3*(8), e1700772. https://doi.org/10.1126/sciadv.1700772

Izutani, Y. (1984). Source parameters relevant to heterogeneity of a fault plane. *Journal of Physics of the Earth*, *32*(6), 511–529. https://doi.org/10.4294/jpe1952.32.511

Ji, C., & Archuleta, R. J. (2020). Two empirical double-corner-frequency source spectra and their physical implications. *Bulletin of the Seismological Society of America*, *111*(2), 737–761. https://doi.org/10.1785/0120200238

Kanamori, H., & Rivera, L. (2004). Static and dynamic scaling relations for earthquakes and their implications for rupture speed and stress drop. *Bulletin of the Seismological Society of America*, *94*(1), 314–319. https://doi.org/10.1785/0120030159

Kaneko, Y., Ampuero, J.-P., & Lapusta, N. (2011). Spectral-element simulations of long-term fault slip: Effect of low-rigidity layers on earthquake-cycle dynamics. *Journal of Geophysical Research*, *116*(B10), B10313. https://doi.org/10.1029/2011JB008395

Kaneko, Y., Lapusta, N., & Ampuero, J.-P. (2008). Spectral element modeling of spontaneous earthquake rupture on rate and state faults: Effect of velocity-strengthening friction at shallow depths. *Journal of Geophysical Research*, *113*(B9), B09317. https://doi.org/10.1029/2007JB005553

Kaneko, Y., & Shearer, P. M. (2014). Seismic source spectra and estimated stress drop derived from cohesive-zone models of circular subshear rupture. *Geophysical Journal International*, *197*(2), 1002–1015. https://doi.org/10.1093/gji/ggu030

Kaneko, Y., & Shearer, P. M. (2015). Variability of seismic source spectra, estimated stress drop, and radiated energy, derived from cohesive-zone models of symmetrical and asymmetrical circular and elliptical ruptures. *Journal of Geophysical Research: Solid Earth*, *120*(2), 1053–1079. https://doi.org/10.1002/2014JB011642

Kano, Y., Kaneko, Y., & Shearer, P. M. (2025). Numerical data for research paper titled "Seismic source spectral properties of dynamic rupture with a self-similar, self-healing slip pulse: Origins of double-corner displacement spectra and implications for small earthquake rupture modes" [Dataset]. *Zenodo*. https://doi.org/10.5281/zenodo.16728573

Ke, C.-Y., McLaskey, G. C., & Kammer, D. S. (2022). Earthquake breakdown energy scaling despite constant fracture energy. *Nature Communications*, *13*(1), 1005. https://doi.org/10.1038/s41467-022-28647-4

Kearse, J., & Kaneko, Y. (2025). Curved Fault slip captured by CCTV video during the 2025 M w 7.7 Myanmar earthquake. *The Seismic Record*, *5*(3), 281–288. https://doi.org/10.1785/0320250024

Komatitsch, D., & Vilotte, J.-P. (1998). The spectral element method: An efficient tool to simulate the seismic response of 2D and 3D geological structures. *Bulletin of the Seismological Society of America*, *88*(2), 368–392. https://doi.org/10.1785/BSSA0880020368

Kostrov, B. (1964). Selfsimilar problems of propagation of shear cracks. *Journal of Applied Mathematics and Mechanics*, *28*(5), 1077–1087. https://doi.org/10.1016/0021-8928(64)90010-3

Lin, Y.-Y., & Lapusta, N. (2018). Microseismicity simulated on asperity-like fault patches: On scaling of seismic moment with duration and seismological estimates of stress drops. *Geophysical Research Letters*, *45*(16), 8145–8155. https://doi.org/10.1029/2018GL078650

Luco, J. E. (1985). On strong ground motion estimates based on models of the radiated spectrum. *Bulletin of the Seismological Society of America*, *75*(3), 641–649. https://doi.org/10.1785/bssa0750030641

Madariaga, R. (1976). Dynamics of an expanding circular fault. *Bulletin of the Seismological Society of America*, *66*(3), 639–666. https://doi.org/10.1785/BSSA0660030639

Madariaga, R. (1977). High-frequency radiation from crack (stress drop) models of earthquake faulting. *Geophysical Journal International*, *51*(3), 625–651. https://doi.org/10.1111/j.1365-246X.1977.tb04211.x

Mayeda, K., & Walter, W. R. (1996). Moment, energy, stress drop, and source spectra of western United States earthquakes from regional coda envelopes. *Journal of Geophysical Research*, *101*(B5), 11195–11208. https://doi.org/10.1029/96JB00112

McGuire, J. J., & Kaneko, Y. (2018). Directly estimating earthquake rupture area using second moments to reduce the uncertainty in stress drop. *Geophysical Journal International*, *214*(3), 2224–2235. https://doi.org/10.1093/gji/ggy201

Melgar, D., & Hayes, G. P. (2017). Systematic observations of the slip pulse properties of large earthquake ruptures. *Geophysical Research Letters*, *44*(19), 9691–9698. https://doi.org/10.1002/2017GL074916

Mello, M., Bhat, H., Rosakis, A., & Kanamori, H. (2010). Identifying the unique ground motion signatures of supershear earthquakes: Theory and experiments. *Tectonophysics*, *493*(3), 297–326. (Earthquake supershear rupture speeds). https://doi.org/10.1016/j.tecto.2010.07.003

Neely, J. S., Park, S., & Baltay, A. (2025). The impact of source time function complexity on stress-drop estimates. *Bulletin of the Seismological Society of America*, *115*(3), 1149–1161. https://doi.org/10.1785/0120240022

Nielsen, S., & Madariaga, R. (2003). On the self-healing fracture mode. *Bulletin of the Seismological Society of America*, *93*(6), 2375–2388. https://doi.org/10.1785/0120020090

Noda, H., Lapusta, N., & Kanamori, H. (2013). Comparison of average stress drop measures for ruptures with heterogeneous stress change and implications for earthquake physics. *Geophysical Journal International*, *193*(3), 169120131712. https://doi.org/10.1785/BSSA0660030639

Prieto, G. A., Shearer, P. M., Vernon, F. L., & Kilb, D. (2004). Earthquake source scaling and self-similarity estimation from stacking P and S spectra. *Journal of Geophysical Research*, *109*(B8), B08310. https://doi.org/10.1029/2004jb003084

Sato, T., & Hirasawa, T. (1973). Body waves spectra from propagating shear cracks. *Journal of Physics of the Earth*, *21*(4), 415–431. https://doi.org/10.4294/jpe1952.21.415

Savage, J. (1972). Relation of corner frequency to fault dimensions. *Journal of Geophysical Research*, *77*(20), 3788–3795. https://doi.org/10.1029/jb077i020p03788

Shearer, P. M., Abercrombie, R. E., & Trugman, D. T. (2022). Improved stress drop estimates for M 1.5 to 4 earthquakes in southern California from 1996 to 2019. *Journal of Geophysical Research: Solid Earth*, *127*(7), e2022JB024243. https://doi.org/10.1029/2022JB024243

Shearer, P. M., Prieto, G. A., & Hauksson, E. (2006). Comprehensive analysis of earthquake source spectra in southern California. *Journal of Geophysical Research*, *111*(B6), B06303. https://doi.org/10.1029/2005jb003979

Shimmoto, S., & Miyake, H. (2025). Resolving the variability discrepancy between peak ground acceleration and spectral stress drop: Insight from double-corner-frequency spectra. *Bulletin of the Seismological Society of America*, *115*(3), 1162–1176. https://doi.org/10.1785/0120240038

Wang, Y., & Day, S. M. (2017). Seismic source spectral properties of crack-like and pulse-like modes of dynamic rupture. *Journal of Geophysical Research: Solid Earth*, *122*(8), 6657–6684. https://doi.org/10.1002/2017JB014454

Ye, L., Kanamori, H., & Lay, T. (2018). Global variations of large megathrust earthquake rupture characteristics. *Science Advances*, *4*(3), eaao4915. https://doi.org/10.1126/sciadv.aao4915

Ye, L., Lay, T., Kanamori, H., & Rivera, L. (2016). Rupture characteristics of major and great (mw2265 7.0) megathrust earthquakes from 1990 to 2015: 2. depth dependence. *Journal of Geophysical Research: Solid Earth*, *121*(2), 845–863. https://doi.org/10.1002/2015jb012427

Yoshida, K., & Kanamori, H. (2023). Time-domain source parameter estimation of Mw 320137 earthquakes in Japan from a large database of moment-rate functions. *Geophysical Journal International*, *234*(1), 243–262. https://doi.org/10.1093/gji/ggad068

Supporting Information for "Seismic source spectral properties of dynamic rupture with a self-similar, self-healing slip pulse: Origins of double-corner displacement spectra and implications for small earthquake rupture modes"

Yuto Kano[1], Yoshihiro Kaneko[1], Peter M. Shearer[2]

[1]Graduate School of Science, Kyoto University, Japan

[2]University of California – San Diego

Contents of this file

1. Text S1: Double corner frequency spectrum predicted from the analytical solution of Sato and Hirasawa (1973)
2. Figures S1 to S14

Text S1: Double corner frequency spectrum predicted from the analytical solution of Sato and Hirasawa (1973)

We observe a double corner frequency at high take-off angles in the crack model based on the approach of Kaneko and Shearer (2014). To investigate whether this phenomenon also manifests in the analytical solution of Sato and Hirasawa (1973), we derive and analyze the corresponding spectrum below.

The analytical solution of Sato and Hirasawa (1973) considers a circular fault with a source radius L. Rupture initiates at $t = 0$ and propagates radially outward at a constant velocity v. Following the framework of Haskell (1964), the displacement components of the far-field P and S waves are expressed as:

$$\begin{aligned} u_r &= \frac{(\beta/\alpha)^3}{4\pi\beta r_0} \sin 2\theta \cos\phi I_\alpha \ , \\ u_\theta &= \frac{1}{4\pi\beta r_0} \cos 2\theta \cos\phi I_\beta \ , \\ u_\phi &= \frac{-1}{4\pi\beta r_0} \cos\theta \sin\phi I_\beta \end{aligned} \tag{1}$$

in polar coordinates (r_0,θ,ϕ), where α and β represent the P- and S-wave speeds, respectively, and r_0 denotes the distance from the fault initiation point to the observation site. The spectral component I_c is defined as:

$$I_c = \begin{cases} 2KvL^2 \left\{\pi/(1-k^2)^2\right\} x^2 & ; 0 < x < 1-k, \\ 2KvL^2(\pi/4) \left\{1/k - x^2/k(1+k)^2\right\} & ; 1-k < x < 1+k, \end{cases} \tag{2}$$

$$\begin{aligned} \tau &= t - r_0/c, \\ x &= v\tau/L \ , \\ k &= (v/c)\sin\theta \ . \end{aligned}$$

The spectral amplitude of $I_c(\tau)$ in Equation (2) is analytically calculated as:

$$|A_c(\omega)| = (M_0/\mu)|B_c(\omega)| \ , \tag{3}$$

where

$$B_c(\omega) = \frac{3}{\omega^2 k(1-k^2)}\left[k\cos(\omega_L k)\cos\omega_L + \sin(\omega_L k)\sin\omega_L + \frac{1}{\omega_L(1-k^2)}\left\{(1+k^2)\sin(\omega_L k)\cos\omega_L - 2k\cos(\omega_L k)\sin\omega_L\right\}\right] + i\frac{3}{{\omega_L}^2 k(1-k^2)}\left[\sin(\omega_L k)\cos\omega_L - k\cos(\omega_L k)\sin\omega_L + \frac{1}{\omega_L(1-k^2)}\left\{2k - (1+k^2)\sin(\omega_L k)\sin\omega_L - 2k\cos(\omega_L k)\cos\omega_L\right\}\right] \quad (4)$$

$$\omega_L = (L/v)\omega\ .$$

The spectral amplitudes of the far-field displacements are given by:

$$\Omega(P,S) = \frac{M_0}{4\pi r_0(\alpha^3,\beta^3)}|R_{\theta_\phi}(P,S)|\cdot|B_c(\omega)|\ , \quad (5)$$

where $R_{\theta_\phi}(P,S)$ represents the radiation patterns of P and S waves for a point source. The normalized spectra are plotted in Figure S7. A double corner frequency spectrum is evident in the S-wave spectra of the model with a rupture speed of $V_r = 0.9\beta$ at a take-off angle of 89.5°.

References

Haskell, N. A. (1964). Total energy and energy spectral density of elastic wave radiation from propagating faults. *Bulletin of the Seismological Society of America*, *54*(6A), 1811-1841. doi: https://doi.org/10.1785/BSSA05406A1811

Kaneko, Y., & Shearer, P. M. (2014). Seismic source spectra and estimated stress drop derived from cohesive-zone models of circular subshear rupture. *Geophysical Journal International*, *197*(2), 1002-1015. doi: https://doi.org/10.1093/gji/ggu030

Sato, T., & Hirasawa, T. (1973). Body Waves Spectra from Propagating Shear Cracks. *Journal of Physics of the Earth*, *21*(4), 415-431. doi: https://doi.org/10.4294/jpe1952.21.415

Yoshida, K., & Kanamori, H. (2023). Time-domain source parameter estimation of Mw 3–7 earthquakes in Japan from a large database of moment-rate functions. *Geophysical Journal International*, *234*(1), 243-262. doi: https://doi.org/10.1093/gji/ggad068

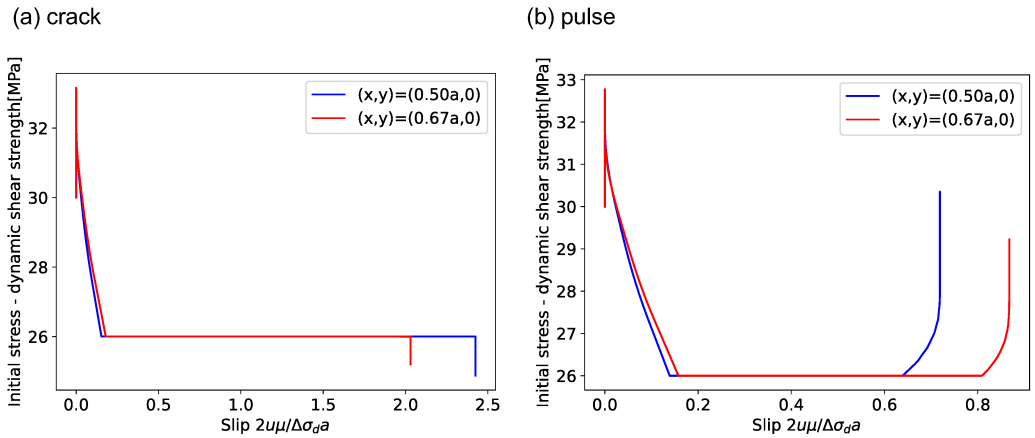

Figure S1. Relationship between local slip and shear stress in our model. The fault is a circular patch with a radius of a, centered at (x, y)=(0, 0). Red and blue lines depict slip-weakening behavior at two points along the Mode II direction. Stress overshoot is observed in the crack model, whereas stress undershoot occurs in the pulse model.

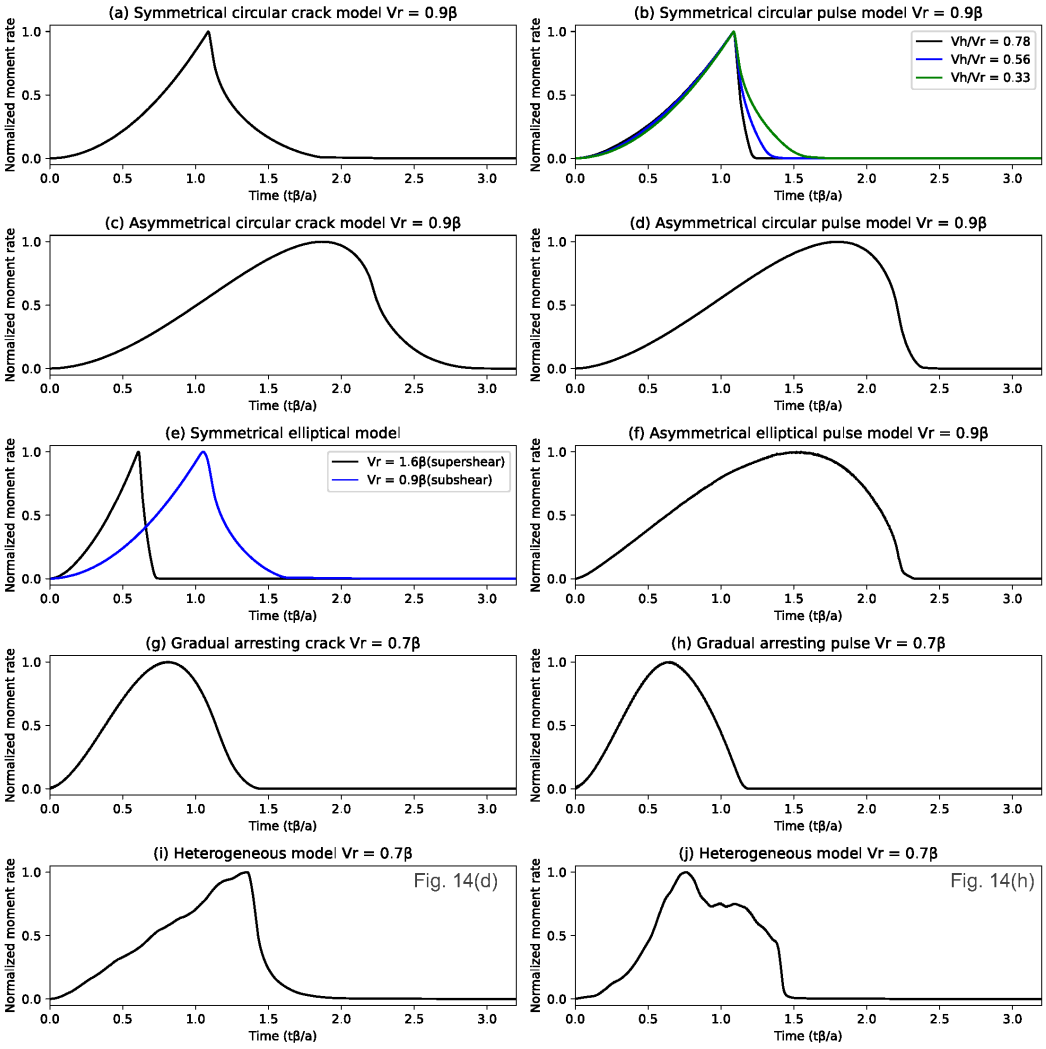

Figure S2. Moment rate functions for the respective source models considered in this study. For the elliptical source models, the source dimension a is replaced with $\sqrt{ab}$. In many cases, the rising part of the moment rate functions follows a t^2 trend, consistent with the model proposed by Sato and Hirasawa (1973).

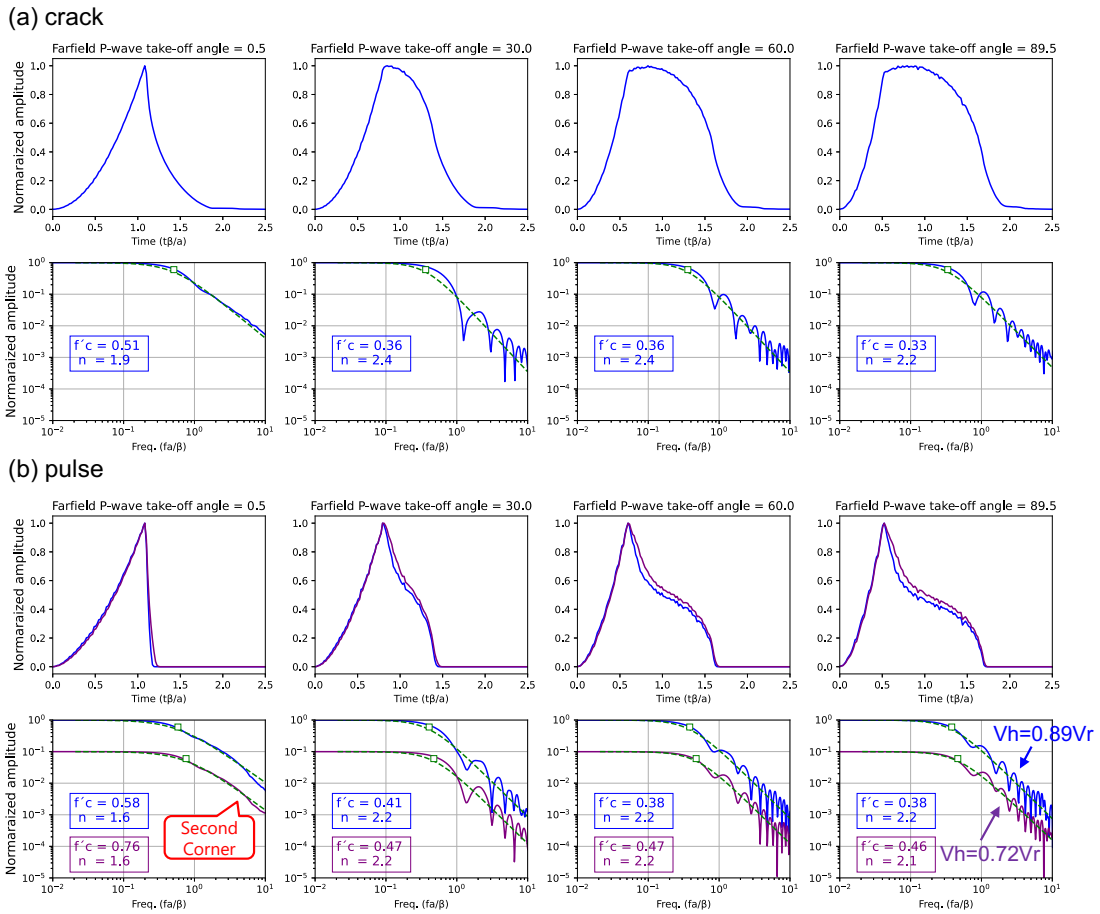

Figure S3. P-wave far-field displacements (upper) and corresponding spectra (lower) at four take-off angles for (a) the crack model with $V_r = 0.9\beta$ and (b) pulse models with $V_r = 0.9\beta$ and $V_h = 0.89V_r$ (blue lines) or $V_h = 0.72V_r$ (purple lines). Corner frequencies are marked by open squares. Green dashed lines represent the best-fitting Brune-type spectral function (Equation 15). Normalized corner frequencies f_c' and fall-off rates n are indicated in the boxes. Only the pulse models at a small take-off angle (0.5°) exhibit double-corner frequency spectra.

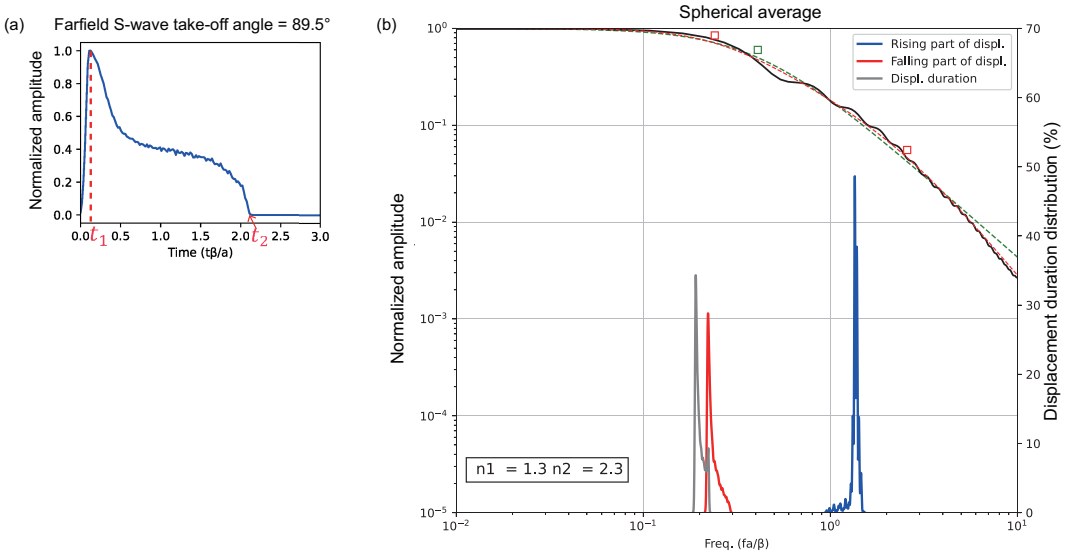

Figure S4. (a) Far-field S-wave displacement at a large take-off angle in the circular pulse model with rupture velocity $V_r = 0.9\beta$ and healing front velocity $V_h = 0.7\beta$, as shown in Figure 8. The peak displacement time (t_1) and total displacement duration (t_2) are indicated. (b) Displacement duration distributions over the focal sphere and stacked spectra for the circular pulse model with rupture velocity $V_r = 0.9\beta$ and healing front velocity $V_h = 0.7\beta$. Three types of displacement duration are shown: the rising part of the displacement (duration t_1, in blue), the falling part ($t_2 - t_1$, in red), and the total displacement duration (t_2, in gray). The duration distribution peaks for the total duration and the rising portion approximately match the first and second corner frequencies (f_{c1} and f_{c2}, respectively) in the stacked spectra. The peak in the duration distribution for the rising part appears slightly lower than the estimated second corner frequency, likely due to an inaccuracy in the spectral fitting process for estimating f_{c2}.

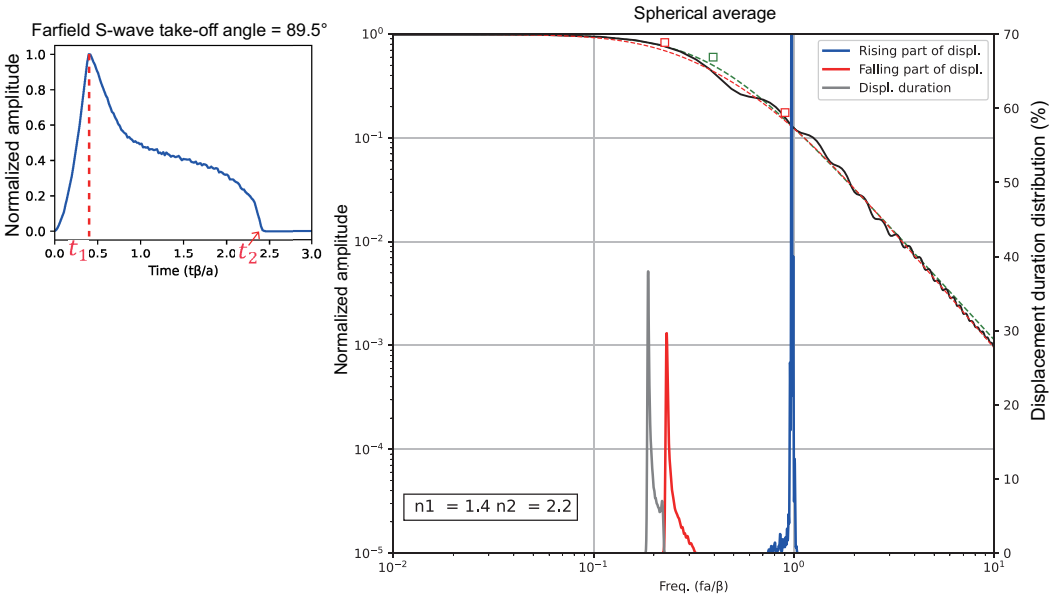

Figure S5. (a) Far-field S-wave displacement at a large take-off angle in the circular pulse model with rupture velocity $V_r = 0.7\beta$ and healing front velocity $V_h = 0.54\beta$, as shown in Figure 8. The peak displacement time (t_1) and total displacement duration (t_2) are indicated. (b) Displacement duration distributions over the focal sphere and stacked spectra for the circular pulse model with rupture velocity $V_r = 0.7\beta$ and healing front velocity $V_h = 0.54\beta$. Three types of displacement duration are shown: the rising part of the displacement (duration t_1, in blue), the falling part ($t_2 - t_1$, in red), and the total displacement duration (t_2, in gray). The duration distribution peaks for the total duration and the rising portion approximately match the first (f_{c1}) and second (f_{c2}) corner frequencies, respectively, in the stacked spectra.

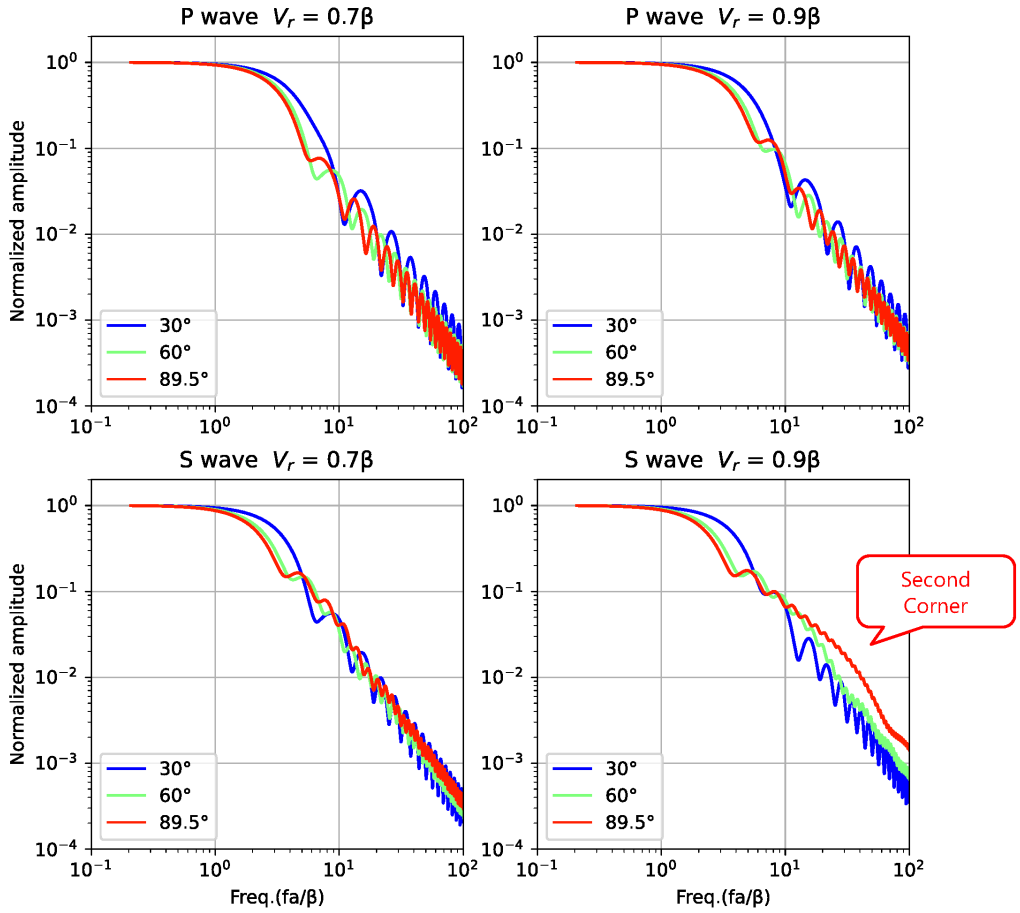

Figure S6. Far-field spectra calculated using the analytical solution of Sato and Hirasawa (1973). Spectra at different take-off angles are shown in different colors. The S-wave spectrum with $V_r = 0.9\beta$ at a take-off angle = 89.5° exhibits prominent intermediate-frequency components, showing a double-corner frequency spectrum caused by rupture directivity effects.

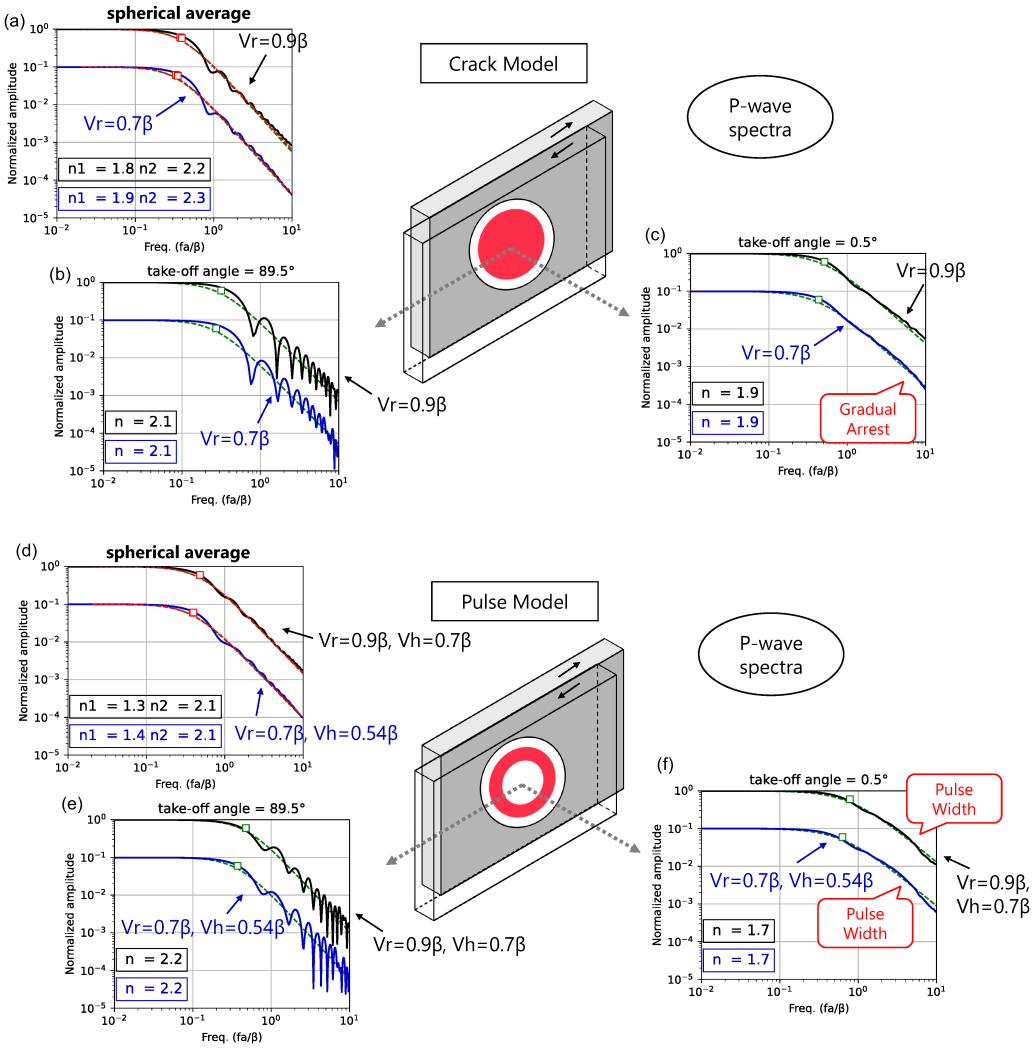

Figure S7. Far-field P-wave displacement spectra for (a-c) circular crack models and (d-f) circular pulse models. (a, d) Stacked spectra over the focal sphere. (b, e) Spectra at take-off angle = 89.5°. (c, f) Spectra at take-off angle = 0.5°. Black lines represent spectra for models with rupture speed $V_r = 0.9\beta$ and the blue ones are $V_r = 0.7\beta$. Spectra for the $V_r = 0.7\beta$ case are uniformly shifted vertically on the logarithmic axis for comparison. The color scheme and indicated values follow those in Figure 8.

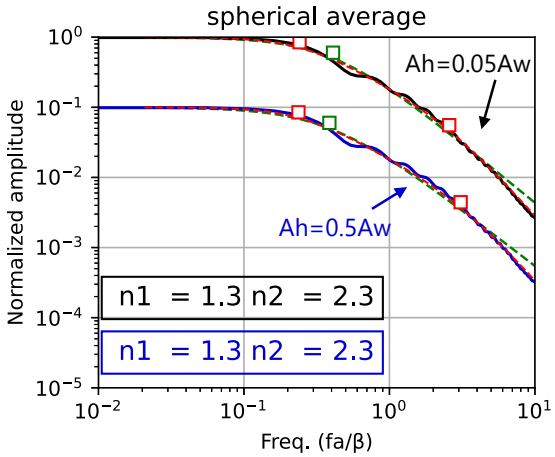

Figure S8. Comparison of spectra for pulse models with different healing rates A_h. The black line represents the spectrum for a pulse model with rupture speed $V_r = 0.9\beta$, healing rate $A_h = 0.05A_w$, while the blue line corresponds to $A_h = 0.5A_w$. Green dashed lines indicate the best-fitting single-corner frequency model (Equation 15), and red dashed lines represent the best-fitting double-corner frequency model (Equation 22). Normalized corner frequencies f_c' and fall-off rates n are indicated. The spectral characteristics of these pulse models are nearly identical.

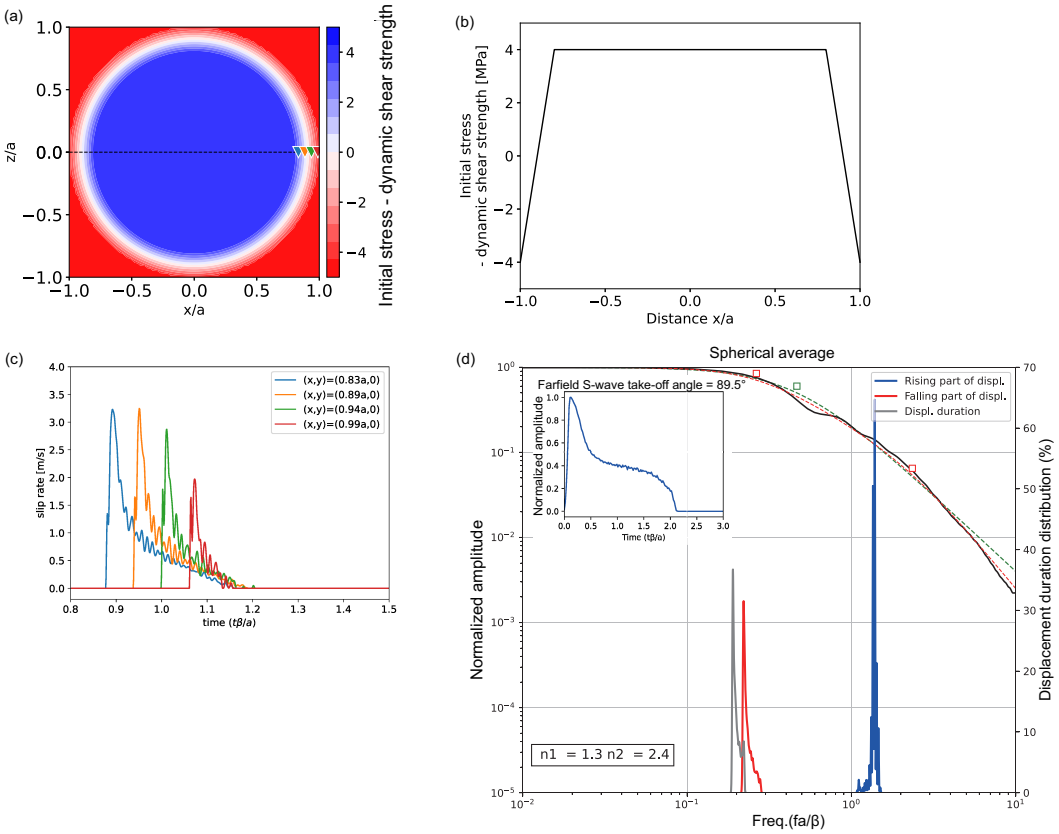

Figure S9. Circular pulse rupture model with gradual arrest, with rupture velocity $V_r = 0.9\beta$ and healing front velocity $V_h = 0.7\beta$. (a) Distribution of initial shear stress minus dynamic shear strength. A transition zone of width $0.2a$ is introduced at the edge of the fault, where the initial shear stress decreases linearly from $\tau_d + 4$ MPa to $\tau_d - 4$ MPa, inducing gradual rupture arrest in this region. (b) Profile of initial shear stress minus dynamic shear strength along the dashed line in panel (a). (c) Slip rates as a function of time at several fault locations indicated in panel (a). (d) Displacement duration distributions over the focal sphere and stacked spectra. Three types of displacement duration are shown: the rising part of the displacement (duration t_1, in blue), the falling part ($t_2 - t_1$, in red), and the total displacement duration (t_2, in gray). The spectral peaks corresponding to the total duration and the rising portion approximately match the first (f_{c1}) and second (f_{c2}) corner frequencies, respectively, in the stacked spectra. While gradual rupture arrest leads to a steeper high-frequency fall-off compared to that in Figure S4, the directivity effects illustrated in Figure 5 remain unchanged, and thus have no significant influence on f_{c2}.

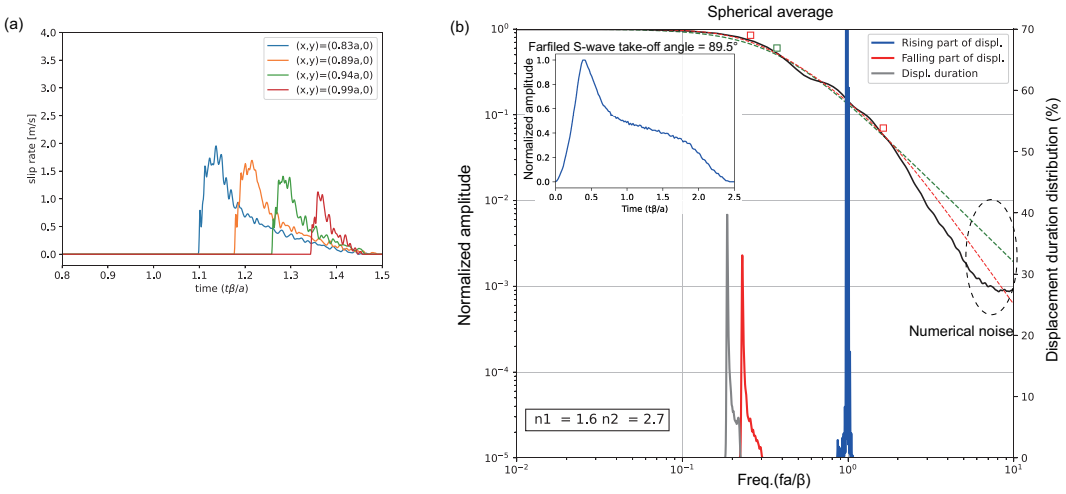

Figure S10. Circular pulse rupture model with gradual arrest, with rupture velocity $V_r = 0.7\beta$ and healing front velocity $V_h = 0.54\beta$. (a) Slip rates as a function of time at several fault locations indicated in Figure S9a. (b) Displacement duration distributions over the focal sphere and stacked spectra. Three types of displacement duration are shown: the rising part of the displacement (duration t_1, in blue), the falling part ($t_2 - t_1$, in red), and the total displacement duration (t_2, in gray). While gradual rupture arrest results in a steeper high-frequency fall-off compared to that in Figure S5, the directivity effects remain unchanged, and thus have no significant influence on f_{c2}.

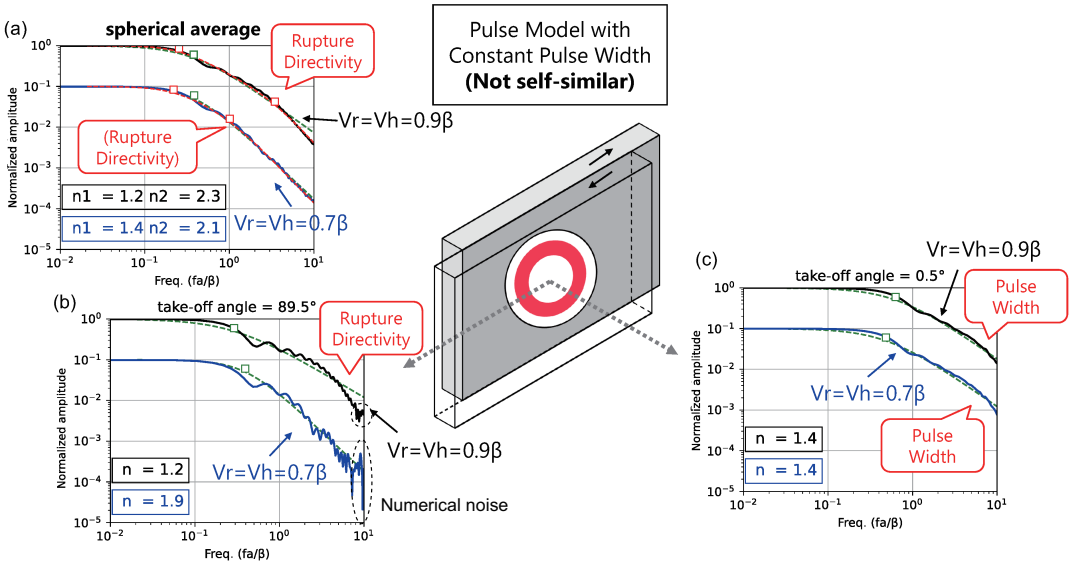

Figure S11. Far-field S-wave displacement spectra for the pulse model with a constant pulse width. (a) Stacked spectra. (b) Spectra at take-off angle = 89.5°. (c) Spectra at take-off angle = 0.5°. Blue lines represent spectra for the model with rupture speed $V_r = 0.9\beta$, while purple lines correspond to $V_r = 0.7\beta$. Green dashed lines indicate the best-fitting single-corner frequency model (Equation 15), and black dashed lines represent the best-fitting double-corner frequency model (Equation 22). Normalized corner frequencies f_c' and fall-off rates n are indicated. The spectral characteristics are consistent with those of the self-similar pulse models.

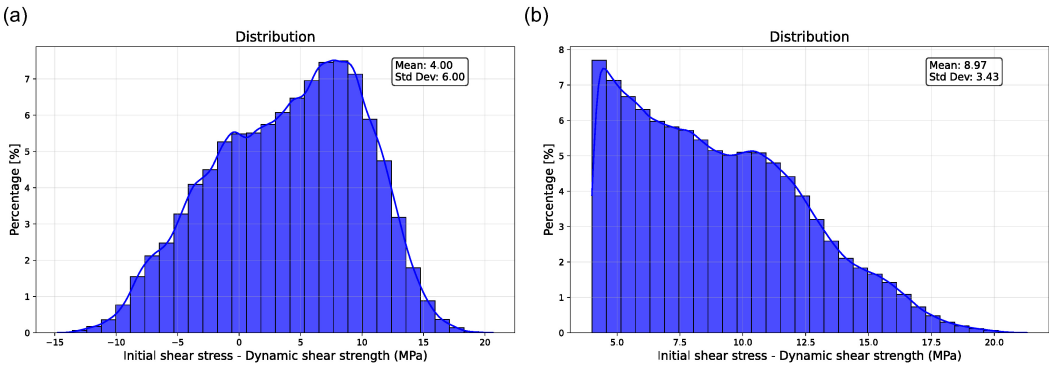

Figure S12. Examples of histograms showing the distribution of initial stress minus dynamic shear strength in the gradual arrest model. (a) Histogram for the model shown in Figure 13a, which exhibits behavior similar to the gradual arrest model. The histogram does not perfectly follow a normal distribution due to the truncation of high wavenumbers during the generation process. (b) Histogram for the model shown in Figure 14e. In this case, values below 4 MPa are removed from the distribution (i.e., the values of initial shear stress minus dynamic shear strength are set to a minimum of 4 MPa), resulting in mean and standard deviation values that differ from 4 MPa and 6 MPa, respectively. In this model, rupture abruptly arrests in regions with very low initial stress, leading to enhanced generation of the stopping phase.

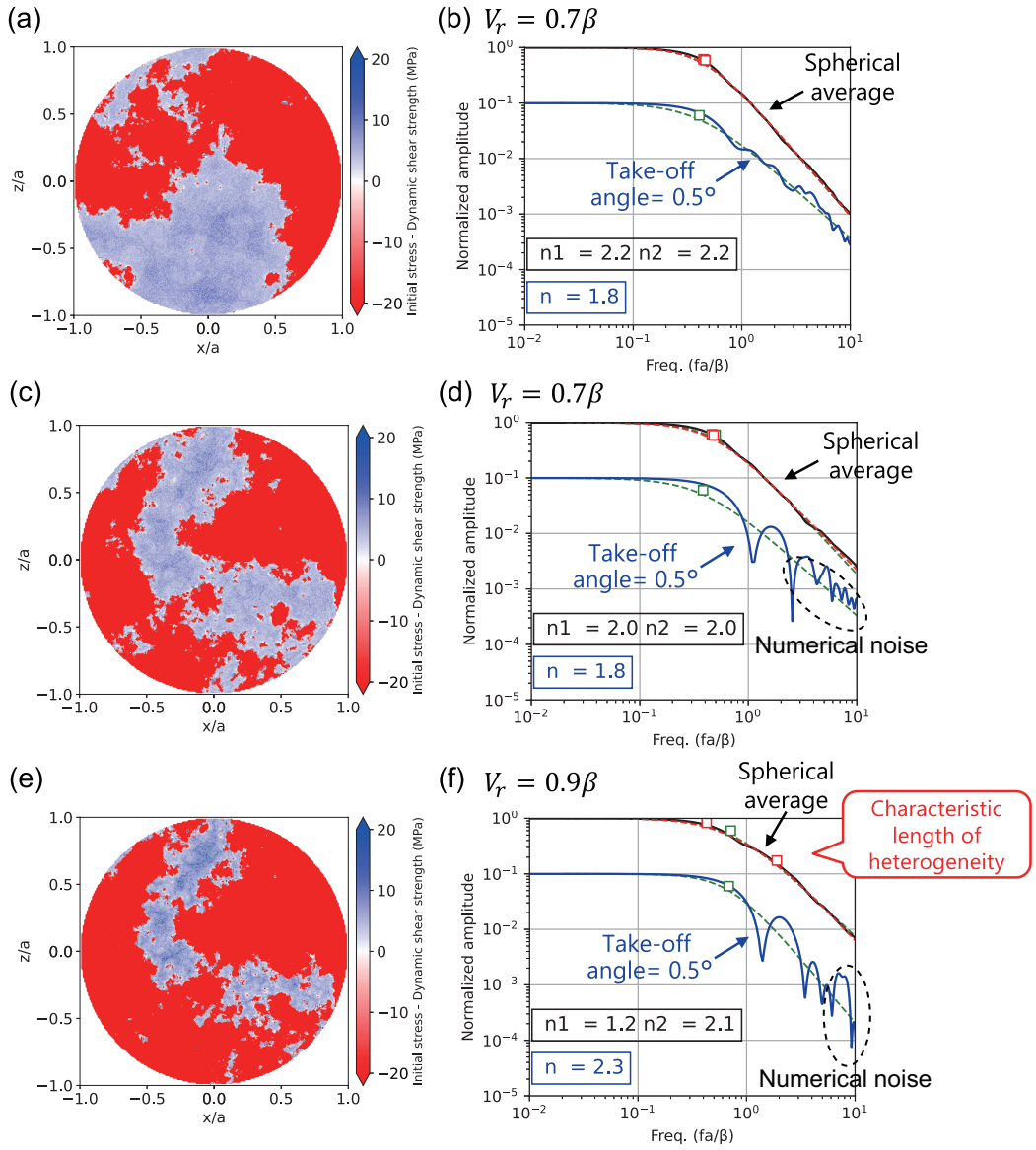

Figure S13. Characteristics of P-wave spectra in two heterogeneous crack models: (a, b) less heterogeneous case, (c, d) more heterogeneous case, and (e,f) more heterogeneous case with a smaller characteristic length. (a, c, e) Initial stress distributions on the fault. (b, d, f) Stacked P-wave spectra (black line) over the focal sphere and spectra at take-off angle = 0.5° (blue line). Spectra are fitted by the single-corner model (red lines) and the double-corner model (green lines), with the corresponding corner frequencies indicated.

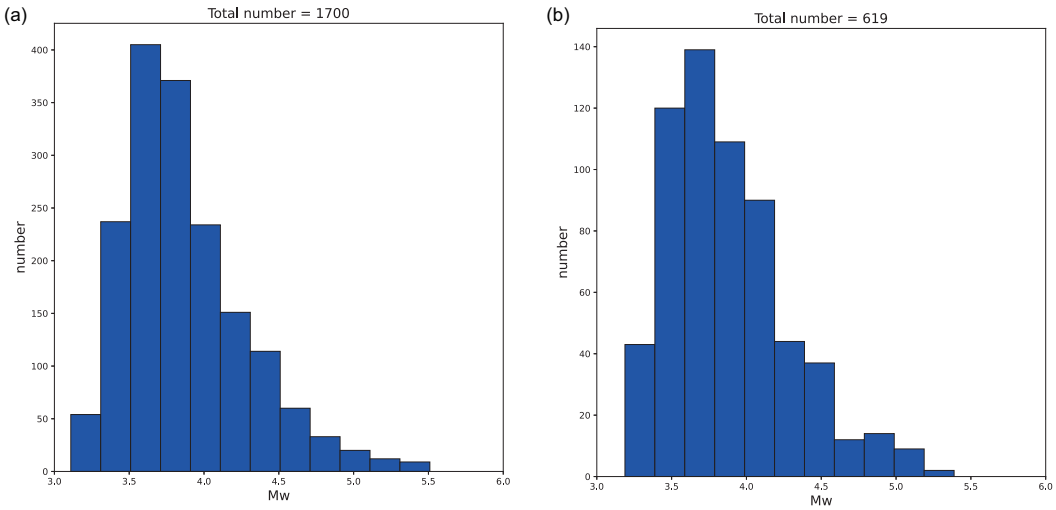

Figure S14. Histograms of moment magnitude (M_w) and earthquake counts based on data from Yoshida and Kanamori (2023). The analysis focuses on events for which source parameters were estimated from velocity seismograms. (a) All events. (b) Events with REEF < 2 and depths shallower than 15 km.